41st Aerospace Sciences Meeting and Exhibit
6-9 January 2003, Reno, Nevada

AIAA 2003-788

AIAA *2003-0788*

Receptivity to Freestream Disturbances of Mach *8* Flow over A Sharp Wedge

Yanbao Ma and Xiaolin Zhong
University of California, Los Angeles

41th Aerospace Sciences Meeting & Exhibit
January 6–9, *2003* / Reno, NV

Receptivity to Freestream Disturbances of Mach 8 Flow over A Sharp Wedge

Yanbao Ma*and Xiaolin Zhong†
University of California, Los Angeles, California 90095

Abstract

In this paper, we continue to study the receptivity mechanisms of supersonic boundary layer to freestream disturbances by using both direct numerical simulation and linear stability theory. The receptivity mechanisms of a Mach 8.0 flow over a sharp wedge with half-angle 5.3° to different freestream disturbances, i.e., fast acoustic waves, slow acoustic waves, entropy waves and vorticity waves, are studied. It is found that the forcing fast acoustic waves do not interact directly with the unstable Mack modes. Instead, the stable mode I waves play an important role in the receptivity process because they interact with both the forcing acoustic waves and the unstable Mack-mode waves. The receptivity mechanisms of the second mode to freestream slow acoustic waves are different from those by freestream fast acoustic waves. The forcing slow acoustic waves can directly generate Mack-mode waves. At small incident angles, slow acoustic waves are more efficient to generate unstable second-mode boundary-layer disturbances than fast acoustic waves. For receptivity to freestream entropy waves or vorticity waves, the generation of boundary-layer disturbances are mainly through fast acoustic waves generated behind the shock due to the interaction between shock waves and freestream disturbances.

Introduction

The transition from laminar to turbulent flow in wall-bounded shear layers occurs because of an incipient instability of the basic flow field, which is identified in stability analyses. In general, the transition is a result of the nonlinear response of the laminar boundary layers to forcing disturbances [1–4]. The forcing disturbances can originate from many different sources, such as freestream turbulence and wall roughness. The forcing disturbances enter the boundary layer as steady or unsteady fluctuations of the basic state, which is called receptivity [5]. The receptivity process, which converts the environmental disturbances into instability waves, such as the Tollmien-Schlichting (T-S) waves, in the boundary layers. The study of the receptivity mechanisms is important because it provides important initial conditions of amplitude, frequency, and phase angles for the instability waves in the boundary layers [6]. The main objective of a receptivity study of a boundary layer is to investigate the properties and mechanisms of initial generation of unstable boundary-layer wave modes by forcing waves.

A Mach 8 flow over a sharp wedge with half-angle 5.3° is studied becaused the same case have been studied by Malik et *al.* [7], but the boundary-layer receptivity mechanisms to freestream disturbances have not been revealed, which requires further parametric studies.

The steady flow solutions are first obtained by using combination of TVD shock-capturing method and shock-fitting method. The detail description of numerical method and code validation are discussed in our previous study [8]. Based the steady flow solutions, characteristics of boundary-layer normal modes at different frequencies are studied by both LST and DNS. At last, the mechanisms of receptivity to four different types of freestream disturbances, i.e., fast acoustic waves, slow acoustic waves, entropy waves and vorticity waves, are studied. The effects of incident wave angles, forcing wave frequencies, on the receptivity are investigated.

Flow Conditions of Mach 8 Flow over a Sharp Wedge

The flow conditions are following Malik *et al.*'s [7] paper:

$$M_\infty = 8.0 \qquad T^*_\infty = 54.78\,K$$
$$p^*_\infty = 389Pa \qquad Pr = 0.72$$
$$Re^*_\infty = \rho^*_\infty U^*_\infty/\mu^*_\infty = 8.2 \times 10^6/m$$

Because the steady flow and geometry are symmetric, only upper half of the flow field is considered in the simulations. Dimensional distance along the wall measured from the leading edge denoted by s^* is used in plotting figures. The dimensional s^* coordinate in the figures can be easily converted to dimensionless local Reynolds numbers according to the following formula:

$$Re_s = Re^*_\infty\, s^* = 8.2 \times 10^6 s^*. \qquad (1)$$

*Graduate Student Researcher, Department of Mechanical and Aerospace Engineering

†Professor, Department of Mechanical and Aerospace Engineering, Associate Fellow AIAA.

In addition, the length scale of boundary-layer thickness L is defined as:

$$L^* = \sqrt{\frac{\mu^*_\infty s^*}{\rho^*_\infty u^*_\infty}}. \qquad (2)$$

Combination of TVD method and shock-fitting method is used in the steady flow computation. The steady flow near the leading edge of the wedge is calculated by TVD method because there exists a singular at the tip of the sharp wedge, which could not be dealt with high order shock-fitting methods. The flow domain for TVD calculation is between $-0.0006m < s^* < 0.0064m$ and the body of wedge start at $x^* = 0.0m$. Uniform grids with $\triangle s^* = 3.5 \times 10^{-5} m$ and totally 200 points are used along streamwise direction (s^*), while 200 points are used in in wall-normal direction (y^*_n) and grid stretching function are used to cluster more points inside the boundary layer near the wall.

The steady flow by using TVD method in the leading edge region are then used as inflow conditions to start the simulation by the fifth-order shock-fitting method. The computational domain of the shock-fitting method is between $0.00409m < s^* < 0.63784m$, or between 3.354×10^4 and 5.23×10^6 in term of Re_s, or between 183.1 and 2287.0 in term of R. In simulation by shock-fitting method, uniform grids with $\triangle s^* = 2.5 \times 10^{-4} m$) aiid totally 2536 points are used in s^*direction, while 121 points and grid stretching function are used in wall-normal direction (y^*_n).

The computational domain is divided into 13 zones and 41 points are used in the overlap region between two neighboring zones. Adiabatic wall boundary condition is used for steady flow calculation, while temperature perturbations on the wall surface are set to be zero for unsteady calculations.

Steady base flow solutions

The steady base flow is calculated by combination of TVD method and shock-fitting method. Figure 1 compares the steady density contours obtained from the TVD method and those from the fifth-order shock-fitting method. The inflow coiidition obtained from the results of TVD method has been validated in many cases of supersonic and hypersonic steady flow over flat plates at Mach numbers ranging from 4.5 to 9.6 in our previous study [8]. For the current case, there is excellent agreement between solutions of the TVD method and high-order shock-fitting method in the overlap region. Again, it shows that the results from TVD method can provide effective inflow conditions for shock-fitting methods.

Figure 2 shows contours of pressure for steady base flow over the wedge calculated by fifth-order shock-fitting method. The upper boundary presents the position of the shock. Compared with Mach 4.5 flow over a flat plate [8], the shock is pushed more close to the wall surface. Inside the flow field, pressure is almost constant across the boundary layer and along the Mach lines.

The distribution of pressure along the wall surface is shown in Fig. 3. There are great pressure gradients resulting from interaction between inviscid external flow and viscous boundary-layer flow near the leading edge. Pressure becomes almost constant in the region downstream where this kind of interaction becomes weaker and weaker.

Figure 4 provides the shock position and distribution of Mach number behind the shock. The shock angle decreases from 14.8' to 11.4°, while Mach number behind the shock increases from 5.91 to 6.72. From inviscid hypersonic flow over a wedge with 5.3' half-angle, the shock angle is 11.10°, Mach number behind the shock is 6.80, and the pressure behind the shock is $p_2 = 2.60$. In the simulation, pressure immediately behind the shock decreases to 2.69 near the exit of the computational domain. Therefore, the results of shock angle, Mach number and pressure behind the shock from the simulation approach the inviscid solutions in the region downstream where shock moves far away from the boundary layer and the interaction between inviscid flow and the viscous boundary layer becomes negligible.

Boundary-Layer Wave Mode Characteristics

In our previous studies on boundary-layer wave mode characteristics of supersonic flow over a flat plate [8], it was found that the distribution of phase velocities of boundary-layer wave modes is a function of the product of the local Reynolds number (R) and frequency (F). Almost the same distributions of phase velocities $vs\ R * F$ for different boundary-layer wave modes are obtained when F is changed while R is fixed, or when R is changed while F is fixed. In this section, characteristics of boundary-Layer wave modes of Mach 8.0 flow over the wedge is studied by both LST and DNS.

Wave Mode Characteristics by LST

Tlie boundary-layer wave mode characteristics of Mach 8.0 flow over the sharp wedge is first studied by the LST. Figure 5 shows the spectra of eigenvalues for $F = 9.63 \times 10^{-5}$ at station $R = 2287.0$ ($w = R * F = 0.2203$). The relative positions of inode I and the second mode in the spectra are highlighted by circles. When w increases little by little, the relative positions of mode I and the second mode will gradually change. We can track the position of each mode aiid obtain their trajectory at different stations with fixed frequencies. The dotted line in Fig. 5 schematically shows the trajectory and relative location of mode I when w changes from low to high. It shows that mode I starts from continuous spectra on the left side of Fig. 5 and passes across another continuous spectra in the middle with increasing w. In the same way, we can find the tra-

jectory of the second mode and mode 11. Here, mode I and mode II are in fact "multiple-viscous solutions" by Mack [9]. The non-dimensional phase velocity of each normal mode can be calculated as

$$a = \omega/\alpha_r. \tag{3}$$

Figure 6 provides distributions of phase velocities of boundary-layer discrete modes, i.e., mode I, mode II and the Mack modes at different locations in terms of w ($w = \mathrm{R} * F$). Two different fixed frequencies] $\mathrm{F} = 9.63 \times 10^{-5}$ and $F = 6.74 \times 10^{-5}$ are considered respectively. The phase velocities of the fast acoustic wave $(1 + 1/M_\infty)$, entropy/vorticity wave (1), and slow acoustic wave $(1 - 1/M_\infty)$ are also shown in the figure for comparison. It shows that both mode I and mode II originate with an initial phase velocity clost to that of fast acoustic wave $(1 + 1/M_\infty)$. Before these two modes become distinct modes, their eigenvalues merge with the continuous spectra on the left side of Fig. 5. After these two wave modes appear, their phase velocities decrease gradually with increasing w. It's obvious that it is discontinuous for the distribution of phase velocity *vs* w for mode I. In Fig. 5, the trajectory of mode I passes across continuous spectra in the middle. In fact, mode I merges with this continuous spectra. Later, another eigenvalue from this continuous spectra becomes discrete mode I. Therefore, there is a gap in the phase velocity curve of mode I. With increasing w, the phase velocity of mode I continues to decrease and passes across the phase velocity curve of Mack modes. At the intersection point ($w = 0.114$), mode I gets synchronized with the second mode, where both modes have very similar profiles of eigenfunctions. A very similar phenomena happens to mode II, including discontinuity in distribution of phase velocity and synchronization with Mack modes, in the region downstream of the computational domain. Unlike mode I, the phase velocity of Mack modes approaches $1 - 1/M_\infty$ near the leading edge, aiid gradually increases with increasing w before the synchronization with mode I waves. After the synchronization point, the phase velocity of Mack modes decreases for a small span of w and then continue to increase. Figure 6 also shows that the distribution of phase velocities of boundary-layer wave modes is a function of the product of the local Reynolds number (R) and frequency (F) Almost the same distributions of phase velocities of boundary-layer wave modes *vs* w ($w = \mathrm{R} * \mathrm{F}$) are obtained for two different frequencies.

The growth rates (a_i) of different normal modes are most important issue in the study by the LST. Figure 7 shows the growth rates of boundary-layer normal modes *vs* w for two different frequencies. Again, the growth rate curves for different normal modes are very close to each other for the two frequencies. While the growth rates of Mack modes are continuous, there is a gap in the growth rate curves for mode I. It also shows that both mode I aiid mode II are stable modes. Mack modes is stable or slightly unstable before the synchronization with mode I ($w < 0.114$). The Mack mode in this range is the conventional first mode. When $w > 0.114$, the Mack mode is the conventional second mode, and the growth rates of the second mode change dramatically. The growth rates of the second mode change from slightly unstable at $w < 0.114$ to most unstable with maximumgrowth rates $\alpha_i = -0.0033$ at $w = 0.121$. The second-mode growth rates decrease to zero at Branch II neutral point with the same value $w = 0.167$ for two different frequencies. As found in our previous study [8], the first mode can gradually change to the second mode without obvious transition. Therefore, the first mode and second mode are in fact different sections of a single Mack mode. Because phase velocities of mode I and the first mode approach that of fast acoustic waves and slow acoustic waves near the leading edge respectively, mode 1 is called fast mode and the first mode is called slow mode by Malik *et al.* [7].

Figure 8 shows the neutral curve of Mack modes for Mach 8.0 flow over the sharp wedge. The critical local Reynolds number (R) for boundary-layer instability is 210. To show the property of the second-mode Branch II neutral point at different frequencies, the neutral curve of Mack modes is redrawn in term of w *vs* R in Fig. 9. When R increases from 1000 to 2287, the second-mode Branch II neutral point in term of w increases from 0.158 to 0.167. The relative change of w is less than 6.0%. This result can be used to predict the location of second-mode Branch II neutral point for $R > 1000$.

Wave Mode Characteristics by DNS

In the study of characteristics of boundary-layer discrete modes of by the LST, the nonparallel effects of the boundary layer, the resonant interactions between different wave modes, and the effects of the oblique shock on the wave modes have been neglected. The numerical siinulations are based on solving the full Navier-Stokes equations, which are able to capture all these effects neglected by the LST. The characteristics of Mack-mode waves and mode I waves, including development of wave structure, change of phase velocity, growth rates, mode change and resonant interactions are studied in numerical simulations by introducing pure boundary-layer discrete modes from the inlet. At the inlet boundary of the computational domain, the flow is specified as the superposition of the steady base flow and a temporal fluctuations of flow variables with multiple frequencies ω_n, amplitude ϵ, and streamwise wave number α_n, i.e,

$$\phi(x_{in}, y, t) = \bar{\phi}(x_{in}, y) + \Re\{\epsilon \sum_{n=0}^{N} \hat{\phi}_n(y) e^{i(\alpha_{r_n} x_{in} - n\omega_1 t)}\}, \tag{4}$$

where $\phi(x_{in}, y, t)$ represents any of the flow variables, $\hat{\phi}_n$(y) is local amplitude of disturbances for boundary-

layer discrete modes at different frequencies obtained from the LST. In the current test cases, a total of 15 frequencies ($N = 15$), with the lowest frequency of $f_1^* = 14.92kHz$, corresponding to dimensionless frequency of $F_1 = 9.63 \times 10^{-6}$, are considered in numerical simulations. Higher frequencies are integer times of the lowest frequency, *i.e.*, $f_n^* = nf_1^*$, and $F_n = nF_1$. The profiles of disturbances of boundary-layer normal modes from the LST are normalized by pressure perturbations on the wall. Therefore, the amplitude of pressure perturbations on the wall of the inlet are same for different frequencies. The factor ϵ to control the total amplitudes of forcing disturbances is carefully chosen so that the nondimensional amplitudes of the perturbations are at least one order of magnitude larger than that of the maximum numerical noise, and they are small enough to avoid nonlinearity of boundary-layer disturbances. Here, $\varepsilon = 1.0 \times 10^{-6}$ is used. The subsequent downstream propagation of boundary-layer normal modes are simulated by time-accurate computations of the full Navier-Stokes equations. The unsteady calculations are carried out until the solutions reach a periodic state in time. Temporal Fourier analysis is carried out on local perturbations of unsteady flow variables to decompose boundary-layer wave modes with different frequencies. The Fourier transform for the real disturbance functions lead to:

$$\phi'(x,y,t) = \Re\{\sum_{n=1}^{N} |\phi_n'(x,y)|\, e^{i[-n\omega_1 t + \psi_n'(x,y)]}\} \qquad (5)$$

where $n\omega_1$ is the frequency of the n-th wave mode, $\phi'(x,y,t)$ represents any flow variables, $|\phi_n(x,\mathrm{y})|$ and $\psi_n'(x,\mathrm{y})$ are real variables representing the local perturbation amplitude and phase angle of the n-th wave mode. These variables indicate a local growth rate α_{rn} and a local wave number α_{in} of the perturbation for the n-th wave mode can be calculated by,

$$\alpha_{rn} = \frac{d\psi_n'}{ds} \qquad (6)$$

$$\alpha_{in} = \frac{1}{|\phi_n'|}\frac{d|\phi_n'|}{ds} \qquad (7)$$

where the derivatives are taken along a grid line parallel to the body surface.

Behavior of Mack modes

Figure 10, 11 and 12 compare amplitudes of pressure perturbations along the wall surfaces between different frequencies, when the first-mode waves are introduced to the flow field from the inlet at $s_{in}^* = 0.02784m$ ($R_{in} = 477.8$). The initial amplitudes of pressure perturbation of the first-mode waves have the same value 8.96×10^{-5} for different frequencies. Except for near the region close to the inlet, Mack-mode waves are amplified in different degrees for different frequencies before they reach maximum amplitudes at the second-mode Branch II neutral points. The reason for the decay of Mack-mode waves at low frequencies is due to the stable properties of the first mode at low local Reynolds number. Among Mack-mode waves with different frequencies, boundary-layer disturbances at frequency with $n = 6(84.53kHz)$ are *most* strongly amplified. For frequencies equal to or lower than $84.53kHz$ ($n \leq 6$), the second-mode Branch II neutral points are located outside of current computational domain. For high frequencies ($n \geq 7$), Mack-mode wave decay after they pass the second-mode Branch II neutral points. Here, growth ratio K_g is defined as the ratio between maximum amplitude of Mack-mode waves at the second-mode Branch II neutral points and initial amplitude at the inlet,i,e.,

$$K_g = \frac{|p'|_{II}}{|p'|_{in}} \qquad (8)$$

Table 1: Second-mode waves at Branch II neutral point ($R_{in} = 477.8$).

n	$f_n^*(kHz)$	K_{gn}	$s_{II}^*(m)$	ω_{II}
7	104.5	157.0	0.5418	0.1422
8	119.4	60.5	0.4067	0.1408
9	134.3	36.8	0.3173	0.1398
10	149.2	24.4	0.2557	0.1395
11	164.1	17.3	0.2084	0.1391
12	179.1	12.9	0.1753	0.1386
13	194.0	9.9	0.1491	0.1385
14	208.9	7.8	0.1285	0.1384
15	223.8	6.3	0.1103	0.1375

Table 1 provides growth ratios and locations of the second-mode Branch II neutral points (s_{II}^* or ω_{II}) for different frequencies.

From table 1, the second-mode Branch II neutral points are located at about $\omega_{II} = 0.140$, and the relative change in terms of w ($w = \mathrm{R} * \mathrm{F}$) from the simulations is less than %3.4, although corresponding value from the LST is about 0.167 and there is much difference between the results from DNS and LST. The growth ratio (k_g) monotonically decreases with increasing frequencies shown in table 1. It should be noted that there are oscillation in amplitude of pressure perturbations in the region downstream after $s^* > 0.32$ for high frequencies within $n \geq 13$ shown in Fig. 12. These oscillations results from high-order harmonics for frequencies within $6 \leq n \leq 8$, because the second-mode waves are strongly amplified at these frequencies. If so, there should be oscillation at frequency with $n = 12$ in downstream too. In fact, there is indeed oscillation at this frequency in downstream if we zoom in distribution of disturbance amplitude in this region. However, the second-mode waves at frequency with $n = 12$ is

Table 2: Second-mode waves generated from mode I waves ($R_{in} = 477.8$).

n	f_n^* (kHz)	K_{gn}	$s_{II}^*(m)$	ω_{II}
7	104.5	12.5	0.5418	0.1429
8	119.4	3.24	0.4067	0.1403
9	134.3	3.48	0.3173	0.1395
10	149.2	0.73	0.2557	0.1391
11	164.1	1.74	0.2084	0.1376
12	179.1	0.90	0.1753	0.1397
14	208.9	0.64	0.1285	0.1406
15	223.8	0.71	0.1103	0.1373

still strong comparing with high-order harmonics from lower frequencies. Thus, oscillation at this frequency in downstream is not visible. Furthermore, this kind of oscillation takes place in downstream region and has no effect on peak amplitude of the second-mode waves at high frequencies between $11 \leq n \leq 15$ located at the second-mode Branch II neutral points, where the amplitude of the second-mode waves at middle frequencies between $6 \leq n \leq 8$ are not fully amplified and high-order harmonics are negligible.

Behavior of mode I waves

After studying the behavior of Mack mode waves, similar studies are carried out for mode I waves. Mode I waves with initial amplitudes 8.96×10^{-5} for pressure perturbations at different frequencies are introduced to the flow field from the same inlet at $s_{in}^* = 0.02784m$ ($R_{in} = 477.8$). Figures 13, 14 and 15 compare amplitudes of pressure perturbations along the wall surfaces between different frequencies. Although mode I waves are predicted to be stable by the LST, there are much more complicated patterns of growth and decay during the propagation of mode I waves compared with the behavior of Mack mode waves shown in Fig. 10, 11 and 12. There are strong oscillations in pressure perturbations for low frequencies ($n < 5$, Fig. 13), which indicates there is modulation between forcing mode I waves and other waves. From pervious study on Mach 4.5 flow over a flat plate [8], the growth and oscillation of mode I waves result from resonant interactions between mode I waves and fast acoustic waves. At higher frequencies ($n \geq 6$), the patterns of growth and decay of boundary-layer disturbances far away from the inlet shown in Fig. 14 and 15 are very similar to the development of Mack mode waves shown in Fig. 11 and 12, which implies the generation of Mack mode waves from mode I waves. This is confirmed by comparison of wave structures in numerical siinulations with the profiles of the second mode from the LST. Table 2 provides growth ratios and locations of the second-mode Branch II neutral points (s_{II}^* or ω_{II}) for different frequencies.

From table 2, the second-mode Branch II neutral points are located at about $\omega_{II} = 0.140$, and the relative change in terms of w ($\omega = \mathrm{R} * \mathrm{F}$) from the simulations is less than %5. Unlike the trend of growth ratio for different frequencies shown in 1, the growth ratio does not monotonically decrease with increasing frequencies from table 2. This is because the second-mode waves are generated by mode I waves. There are resonant interactions between mode I waves and fast acoustic waves, which can be effected by phase velocity, phase angle and frequency of mode I waves. Unlike that growth ratio and growth rates of Mack-mode waves only depend on frequency, there are many factors which can effect the growth of mode I waves. Therefore, Mack-inode waves generated from mode I waves can also be effected from these factors besides of frequency. For very high frequencies ($n \geq 11$, Fig. 15), there are visible oscillations in pressure perturbations after the second Mack-mode waves decay. This kind of oscillation is different from that shown in Fig. 12, where oscillations looking like numerical noise with tiny wavelength result from high-order harmonics with lower frequencies. In Fig. 15, oscillations are due to modulations between the second-mode waves and other waves inside the boundary layer. In addition, the amplitudes of the second-mode waves generated by mode I waves at middle frequencies between $6 < n < 8$ shown in Fig. 14 are one order of magnitude less the amplitudes of second-inode waves shown in Fig. 11. Therefore, effect from high-order harmonics is small in Fig. 15.

Comparison with LST

The results about behavior of Mack-mode waves and mode I waves from numerical simulations are compared with LST for three typical frequencies, $F = 5.78 \times 10^{-5}, 6.74 \times 10^{-5}$ and $6.93 \times 10^{-5} (n = 6, 7, 10)$.

Figure 16 compares the phase velocities of boundary-layer disturbances at frequency $\mathrm{F} = 6.74 \times 10^{-5} (n = 7)$ with the LST results. There is good agreement in phase velocity of Mack modes between DNS and the LST. However, for mode I waves, there are strong oscillations in phase velocity curve, which is due to modulation between mode I waves and fast acoustic waves. In fact, there are strong fast acoustic wave components outside the boundary layer in tlie initial mode I waves at tlie inlet, which has been demonstrated in our previous study [8]. In addition, at the inlet location where mode I waves are introduced to the flow field, phase velocity of mode I is very close to that of fast acoustic waves ($1 + 1/M_\infty$). Therefore, there is resonant interaction between mode I waves and fast acoustic waves. As a result, mode I waves are modulated and amplified. During propagation downstream, the phase velocity of mode I waves gradually decreases. When the phase velocity of inode I waves becomes far away from that of fast acoustic waves, there are no more resonant inter-

actions between them and mode I waves decay due to their inherent, stable properties (see Fig. 15). Before inode I waves die out, their phase velocity gets synchronized with that of Mack modes. Both tlie first Mack-inode waves and mode I waves have almost the same profiles of disturbance structure across the boundary layer at the synchronization point according to our previous study [8]. As a result, mode I waves convert to the Mack-mode waves in the synchronization region, which is shown in the distribution of pressure perturbation on tlie wall (Fig. 14 and 15) and comparison of phase velocity curves in Fig. 16. There is no more oscillations in phase velocity curve after mode I waves convert to Mack mode waves because Mack-mode waves are significantly amplified and become dominant modes due to their unstable properties.

A similar analysis is carried out for the frequency with $n = 10$ (149.2 kHz). As shown in Fig. 14, mode I waves at frequency with $n = 10$ is less amplified and decays to much smaller amplitude before they converts to Mack-mode waves, compared with tlie behavior of mode I waves at lower frequency with $n = 7$. This can be explained from the change of phase velocity of mode I waves shown in Fig. 17, where phase velocities of boundary-layer disturbances at frequency $F = 9.63 \times 10^{-5}$ from the simulation are compared with the LST results. Overall, the trend of phase velocities shown in Fig. 17 for frequency with $n = 10$ is very similar to that shown in 16 for $n = 7$. Good agreement is obtained for both mode I waves and Mack-mode waves between DNS and LST. The gap in phase velocity curve of inode I waves from the LST does not show in the results from DNS. In other words, there is no much effect from gap in phase velocity curve of mode I waves from the LST. The phase velocity of mode I waves shown in Fig. 17 decrease much faster compared with that shown in 16 for lower frequency case. Therefore, there is shorter range of resonant interaction between mode I waves and fast acoustic waves at frequency with $n = 10$ compared with lower frequency ($n = 7$). This is why mode I waves at frequency with $n = 10$ is less amplified and decays to much smaller amplitude before they converts to Mack-mode waves, compared with the behavior of mode I waves at lower frequency with $n = 7$ as shown in Fig. 14.

Growth rates of boundary-layer normal modes are most important properties in the stability study. Figure 18 compares tlie growth rates of Mack-mode waves at three different frequencies ($n = 6, 7, 10$) froin numerical simulations with the LST results. There is good agreement near tlie peak growth rates between DNS and LST for different frequencies. However, there is much difference between LST and DNS in growth rates far away from tlie peak value. Parallel flow assumption in the LST is one possible reason for the difference. In fact, the effect from parallel flow assumption is negligible in the region downstream. In addition, oblique shock moves far away from the boundary layer in downstream region too. Therefore, the effect from the oblique shock can not be the main reason for this difference either. DNS accounts for both nonparallel and nonlinear effects, so tlie growth rates from the results of DNS should be more reliable, although the real reason for tlie difference between DNS and LST is not clear.

Receptivity to Freestream Acoustic Waves

Having studied the characteristics of boundary-layer normal modes, freestream acoustic waves are introduced to study receptivity phenomenon that is the process how environment disturbances enter boundary layer and trigger instability waves. In this section, receptivities to both freestream fast and slow acoustic waves with different frequencies and incident angles are studied. Boundary-layer disturbances induced from freestream acoustic waves are identified by comparison with LST results. For purpose of comparison, receptivity to freestream fast acoustic waves is discussed together with that to freestream slow acoustic waves.

Acoustic Waves with $\theta_\infty = -5.3°$, $F = 6.46 \times 10^{-5}$

Figure 19 shows contours of instantaneous pressure perturbations induced by freestream plane fast acoustic waves (a) and slow acoustic waves (b), respectively. In both test cases, acoustic waves with frequency $F = 6.46 \times 10^{-5} (f^* = 100kHz)$ amplitude $\varepsilon = 10^{-5}$ and orientation angle $\theta_\infty = -5.3°$ are considered. At this incident angle, the propagation direction of freestream acoustic waves is parallel to the wedge wall surface. Only part of tlie flow field is shown for clarity. Before acoustic waves entering the boundary layer, they are first processed by the shock wave. Due to different phase velocities between fast and slow acoustic waves, tlie transmitted wave patterns behind the shock are different in these two cases, which is shown in Fig. 19. After transmitted acoustic waves penetrate tlie boundary layer, different patterns of boundary-layer disturbances are generated. The main difference in patterns of boundary-layer disturbances is that there is boundary-layer mode change located near $x^* = 0.33m$ for those induced by fast acoustic waves. Such boundary-layer inode change does not shown in boundary-layer disturbances induced by slow acoustic waves (Fig. 19 (b)). All different components of boundary layer disturbances induced by freestream acoustic waves will be identified by comparison with LST later.

The induced pressure perturbations on the wall are compared in Fig.20. It's obvious that pressure perturbations induced by slow acoustic waves are much stronger than that by fast acoustic waves at current flow conditions. A portion of Fig. 20 near tlie leading edge is reproduced in Fig. 21 to highlight the initial evolution of boundary-layer disturbances induced by freestream acoustic waves. While the amplitude of boundary-layer

disturbances induced by slow acoustic waves monotonically increase, the amplitude of boundary-layer disturbances induced by fast acoustic waves goes through a growth region first ($s^* < 0.19m$), then a decay region ($0.19m < s+ < 0.34m$), followed by a growth region again afterward ($s^* > 0.34m$). Unlike that there is smooth growth in disturbances by slow acoustic waves, there is modulation in disturbances induced by fast acoustic waves. To identify the dominant component in boundary-layer disturbances, the structure of boundary-layer disturbances at station $s^* = 0.1178m$ (R = 1207.6) are compared with eigenfunctions of boundary-layer normal modes from the LST. Figure 22 present the comparison of wave structure from the simulation for fast acoustic waves with profiles of mode I waves at the same location, while figure 23 compare the wave structure from the simulation for slow acoustic waves with profiles of the first-mode waves. From the comparison, the profiles of boundary-layer disturbances from fast acoustic waves can math the profiles of mode I waves, and boundary-layer disturbances from slow acoustic waves match the profiles of the first-mode waves from the LST. In other words, mode I waves are generated by fast acoustic waves, while the first-mode waves are generated by slow acoustic waves.

The mechanism of generation of different boundary-layer normal modes by fast acoustic waves and slow acoustic waves are clearly shown in distribution of phase velocity of boundary-layer disturbances presented in Fig. 24. The phase velocities of boundary-layer normal modes from the LST are compared with the results from DNS. In receptivity to freestream fast acoustic waves, the phase velocity of boundary-layer disturbances near the leading edge from the simulation is close to that of mode I from the LST, which indicates that mode I waves are generated by fast acoustic waves. From our previous study on characteristics of boundary normal modes, mode I waves are amplified due to resonant interactions with the forcing fast acoustic waves because their phase velocities are very close to each other near the leading edge. During propagation downstream, the phase velocity of mode I waves gradually decreases. When phase velocities of mode I waves decrease to a certain value and there is no more resonant interaction between mode I waves and fast acoustic waves ($s^* > 0.19m$), mode I waves decay due to their inherent stable properties. Before they die out, mode I waves convert to the Mack-mode waves in the synchronization region between mode I waves and the first-mode waves. This can explain the mode change shown in Fig. 19(a). Mack-mode waves generated by mode I waves are strongly amplified due to the instability of Mack-mode waves. On the other hand, in receptivity to freestream slow acoustic waves, the first Mack mode waves are generated due to resonant interactions between the first-mode waves and the forcing slow acoustic waves. Due to slightly unstable property of the first-mode waves and significantly unstable property of the second-mode waves, boundary-layer disturbances generated from the slow acoustic waves are strongly amplified. Because of different receptivity mechanisms shown in Fig. 24, boundary-layer disturbances induced by slow acoustic waves are much stronger than that by fast acoustic waves at current flow conditions. For quantitative analysis, the response coefficients of the boundary-layer normal mode is defined as ratio of maximum amplitude of the boundary-layer normal mode to that of freestream disturbances, i.e,

$$K_{mode} = \frac{|p'_{mode}|}{|p'_{\infty}|}, \tag{9}$$

where $|p'|_{mode}$ is the maximum amplitude of pressure perturbations for the given wave mode. For the second mode, this maximum value is located at the Branch II neutral point. The response coefficients of the second mode are 434.9 and 40.1 for fast and slow acoustic waves, respectively. The second-mode Branch II neutral point in term of ω is located at 0.1438 from the simulations. Therefore, the receptivity to slow acoustic waves are 10 times stronger than the to fast acoustic waves for the current cases. The reason for this big difference in the second mode between receptivity to fast and slow acoustic waves is because different boundary-layer disturbances are generated near the leading edge. Mode I waves are generated in receptivity to fast acoustic waves while the first Mack mode waves are generated by slow acoustic waves near the leading edge. Mode I waves are much stable than the first Mack mode. As a result, the initial amplitude of the second Mack mode converted from mode I waves is much weaker than that from the first Mack mode. Therefore, the peak amplitude of the second mode waves are much weaker in receptivity to fast acoustic waves compared with that to slow acoustic waves.

The same case of hypersonic boundary-layer response to freestream fast acoustic waves has been studied by Malik *et al.* [7]. It was concluded that both the slow mode with phase speed close to $1-1/M_{\infty}$ and fast mode with phase speed close to $1+1/M_{\infty}$ were generated by fast acoustic waves. The fast mode eventually died out while the slow mode grew to large amplitude. From our study, only mode I (fast mode) waves are generated by fast acoustic waves near the leading edge. There is no slow mode (the first mode) directly generated by fast acoustic waves near the leading edge. Instead, the first-mode (or Mack-mode) waves are generated from mode I waves. The Mack-mode waves are strongly amplified after generation.

Effect of Incident Angles

The effect, of incident acoustic wave angles on receptivity to both planar freestream fast acoustic waves and planar freestream slow acoustic waves is studied

at frequency F = 6.46 x 10^{-5}. Freestreain acoustic waves with four different incident angles, i.e., $\theta_\infty = -5.3°, 17.2°, 39.7"$ and 62.2" are considered. The amplitude of the velocity disturbance in freestream is chosen to be $\epsilon = 1.0 \times 10^{-5}$.

Figure 25 compares amplitudes of pressure perturbations along the wall surface due to planar freestream fast acoustic waves with different incident angles. The general pattern of boundary-layer disturbances by freestream fast acoustic waves is very similar for different incident angles. For different incident angles, there are much difference in the impingement and reflection of transmitted fast acoustic waves, and interaction between inode I waves and fast acoustic waves. All these factors can affect, the boundary-layer receptivity. Among these incident angles studied here, maximum response of the second mode to freestream fast acoustic waves is obtained at $\theta_\infty = 39.7"$ with response coefficient $K_s = 74.5$.

Figure 26 compares amplitudes of pressure perturbations along the wall surface due to planar freestream slow acoustic waves with different incident angles. Again, the general shapes of distributions of boundary-layer disturbances by freestream slow acoustic waves are very siinilar for different incident angles. With increasing incident angle, receptivity to slow acoustic waves drops dramatically, which is also shown in Fig. 27 for response coefficients of the second mode. Meanwhile, the receptivity to fast acoustic waves shown in Fig. 27 is not so very sensitive to change of incident acoustic wave angles compared with that to slow acoustic waves.

Effect of Frequencies

In this section, hypersonic boundary-layer receptivity to free-stream acoustic disturbances with different frequencies is studied for Mach 8.0 flow over the 5.3" half-angle sharp wedge. Both freestream planar fast and slow acoustic waves at $\theta_\infty = -5.3'$ contain 15 frequencies with the lowest frequency of $f_1^* = 14.922kHz$ corresponding to dimensionless frequency of $F_1 = 9.63 \times 10^{-6}$. The perturbations of an arbitrary flow variable in the freestream can be written in the following form:

$$\phi'_\infty(x,y,t) = |\phi'| \sum_n^N A_j \, e^{i[n\ \omega_1(\frac{x}{c_\infty}-t)+\psi'_n]} \quad (10)$$

where $N = 15, |\phi'|A_n$ represents the wave amplitude of the freestream perturbation of any flow variables at a frequency

$$\omega_n = n\ w_1\ , \qquad (n = 1, 2, \cdots, N) \quad (11)$$

where w_1 is the minimum frequency of the waves. The relative amplitude of each ω_n frequency denoted by ***A,*** is given in table 3 and satisfying,

$$\sum_n^N A_n^2 = 1\ . \quad (12)$$

Table 3: Acoustic wave components in the freestream.

n	f_n^* (kHz)	$F_n * 10^6$	A_n	$\phi_n(radian)$
1	14.92	9.63	0.7692	2.4635e-6
2	29.84	19.26	0.4162	0.160
3	44.77	28.89	0.2827	2.2149
4	59.68	38.52	0.2065	4.1903
5	74.61	48.15	0.1707	6.0510
6	84.53	57.78	0.1406	5.2671
7	104.5	67.41	0.1132	2.1070
8	119.4	77.04	9.7164(-2)	5.7511
9	134.3	86.67	0.1081	5.0005
10	149.2	90.35	9.0781(-2)	5.2319
11	164.1	96.30	7.7722(-2)	2.1679
12	179.1	115.56	5.8428(-2)	5.4738
13	194.0	125.19	5.0729(-2)	0.5649
14	208.9	134.82	7.6987(-2)	5.5812
15	223.8	144.45	5.7108(-2)	4.4043

In the equation above, c_∞ is the wave speed in the freestream before reaching the shock. The initial phase angle, ψ'_n, of the forcing acoustic wave at frequency ω_n is determined randomly. The absolute amplitude of the wave group is determined by setting the values $|\phi'|$ according to relations of acoustic waves. The wave frequencies, amplitudes, and phase angles used in the current receptivity simulation are given in table 3. The overall wave amplitude is $\epsilon = 1.0 \times 10^{-4}$ with 15 frequencies ($N = 15$).

Temporal Fourier analysis is carried out on local perturbations of unsteady flow variables after a time periodic state has been reached. The Fourier transform in Eqn. 5 for the real disturbances is used to extract the local perturbation amplitude and phase angle for different frequencies. The wave modes induced by freestream acoustic waves are identified and the growth rates are compared with LST analysis.

Fast acoustic waves at different freauencies

Figure 28, 29 and 30 compare pressure perturbations along the wall surface induced by planar freestream fast acoustic waves at $\theta_\infty = -5.3'$ with different frequencies. It's obvious that there are strong oscillations in boundary-layer disturbances at different frequencies except for $n = 6$, where the boundary-layer disturbances are most strongly amplified. At frequencies within $n \leq 6$, the second-mode Branch II neutral points are outside the computational domain. At very high frequencies within $n \geq 11$, the evolution of the second-inode waves is contaminated by modulation with other waves. The response coefficients of the second mode at frequencies within $7 \leq n \leq 10$ are given in table 4.

From table **4,** it shows that the response coefficients of the second mode decrease with increasing frequency

Table 4: Response coefficients of the second mode to freestream fast acoustic waves.

n	f_n^* (kHz)	K_s	$s_{II}^*(m)$	ω_{II}
7	104.5	44.5	0.54136	0.1420
8	119.4	21.3	0.4226	0.1434
9	134.3	16.7	0.3076	0.1376
10	149.2	15.0	0.2671	0.1425

Table 5: Response coefficients of mode I to freestream fast acoustic waves.

n	f_n^* (kHz)	K_s	$s^*(m)$	w
11	164.1	7.39	0.0896	0.0930
12	179.1	6.86	0.0823	0.0972
13	194.0	7.50	0.0746	0.1003
14	208.9	5.92	0.0473	0.0860
15	223.8	6.09	0.0448	0.0897

from $n = 7$ to $n = 10$. At high frequencies between $11 \leq n \leq 15$, the receptivity of mode I waves are dominant, and response coefficients are given in table 5. While the second-mode response coefficients significantly drop off with increasing frequencies, there are no much changes in those of inode I waves for different frequencies shown in table 5.

Slow acoustic waves at different frequencies

Figure 31, 32 and 33 compare pressure perturbations along the wall surface induced by planar freestream slow acoustic waves at $\theta_\infty = -5.3'$ with different frequencies. Unlike receptivity to fast acoustic waves, there are smooth evolutions of boundary-layer disturbances induced by freestream slow acoustic waves at different frequencies, except that there are visible oscillations in disturbance amplitudes at frequencies between $10 \leq n \leq 15$ in the region downstream with $s^* > 0.25m$, which results from effect of high-order harmonics. Actually, there is no oscillation in the second-mode waves at frequency with $n = 10$ shown in Fig. 11, while that is present in Fig. 32 at the same frequency, because the amplitude of the second-mode waves at frequency with $n = 5$ shown in Fig. 10 is about 6 times smaller than that shown in Fig. 31. As a result, there is effect from high-order harmonics on the second-mode waves at frequency with $n = 10$ in Fig. 31, while this effect is negligible in Fig. 11.

Again, boundary-layer disturbances at frequency with $n = 6$ are most strongly amplified. At frequencies within $n \geq 7$, the response coefficients of the second inode are given in table 6 because the locations of the second-mode Branch II neutral points at frequencies within $n \leq 6$ are outside the computational domain.

Table 6: Response coefficients of the second mode to freestream slow acoustic waves.

n	f_n^* (kHz)	K_s	$s_{II}^*(m)$	ω_{II}
7	104.5	339.9	0.5431	0.1457
8	119.4	155.6	0.4051	0.1438
9	134.3	96.87	0.3171	0.1431
10	149.2	59.56	0.2556	0.1428
11	164.1	41.35	0.2101	0.1424
12	179.1	30.38	0.1758	0.1421
13	194.0	22.80	0.1483	0.1414
14	208.9	18.13	0.1268	0.1408
15	223.8	14.63	0.1111	0.1412

Again, it shows in the table 6 that the second-mode Branch II neutral points are located at about $\omega_{II} = 0.14$, and the relative change in terms of w ($w = R * F$) from the simulations is less than %5. In addition, the second-mode response coefficients decrease as frequency increases.

Figure 34 compares boundary-layer receptivity to freestream fast or slow acoustic waves changing with frequencies. It shows that receptivity to slow acoustic waves at incident. angle $\theta_\infty = -5.3°$ is always much stronger than that to fast acoustic waves at the same frequency and incident, angle.

Comparison with previous results and LST

The results of receptivity to freestream acoustic waves from numerical simulations are compared with previous results obtained by prescribing different eigenfunctions at the inflow and LST results for two typical frequencies, $\mathbf{F} = 6.74 \times 10^{-5} (n = 7)$ and $9.63 \times 10^{-5} (n = 10)$.

Figure 35 compares phase velocity of boundary-layer disturbances induced by freestream fast acoustic waves at frequency with $n = 7$ with LST results. The solutions obtained by prescribing mode I eigenfunctions at the inflow are also plotted here for comparison. As expected, the phase velocity of induced boundary-layer disturbances from fast acoustic waves is close to that of mode I waves from LST results in upstream before Mack inodes are generated from mode I waves. In downstream, phase velocity of boundary-layer disturbances can match that of Mack modes from LST results. Overall, there is better agreement on distributions of phase velocity between the results from receptivity to fast acoustic waves and that obtained by introducing mode I waves from the inlet.

The distribution of phase velocity of boundary-layer disturbances induced by freestream slow acoustic waves at frequency with $n = 7$ is compared with the simulation result of Mack mode introduced from the inlet as well a.s the results from the LST, which is plotted in Fig. 36. There is excellent agreement on distribution of phase

velocity between the results from receptivity to slow acoustic waves and simulation results of Mack modes. Phase velocity curves from both simulation results can match that of Mack modes from the LST.

Figure 37 shows the comparison of growth rates between the results from receptivity to fast acoustic waves at frequency with $n = 7$ and simulation results of Mack modes as well as LST results. There are strong oscillations in growth rates of boundary-layer disturbances induced by fast acoustic waves. Therefore, it is difficult to compare growth rates from receptivity to fast acoustic waves with LST results or numerical results of Mack modes. Base on this result, it is reasonable to imagine that it is difficult to measure the distribution of growth rates of boundary-layer normal modes, especially the second mode, by studying boundary-layer disturbances induced by freestream fast acoustic waves in experiment without decomposition of different disturbance components. It's even more difficult to obtain agreement with that. from the LST.

Unlike receptivity to fast acoustic waves, there is excellent agreement on growth rates between the results from receptivity to slow acoustic waves and numerical results of Mack modes, which is shown in Fig. **38.** However, there is much difference between simulation results and LST results except that maximum growth rates are close between LST and DNS. As stated before, the results of growth rates from numerical simulations should be more reliable than that from LST.

Similar analysis is also carried out for frequency with $n = 10$. Figure 39 compares phase velocity of boundary-layer disturbances induced by fast acoustic waves with simulation results of mode I waves. Again, there is good agreement on distribution of phase velocity between different numerical simulations except that there are much stronger oscillations in the downstream region for the results on receptivity to fast acoustic waves, because there are much stronger modulation between boundary-layer disturbances and forcing fast acoustic waves, compared with the case where boundary-layer disturbances generated by mode I waves forcing from the inflow.

Figure 40 compares phase velocity of boundary-layer disturbances induced by slow acoustic waves with simulation results of Mack modes. Again, there is excellent agreement between results from different simulations. In addition, the simulation results are very close to LST results.

Receptivity to Planar Freestreain Entropy Waves

Beside of freestream acoustic waves, freestream entropy waves are another source of disturbances from the freestream that can induce boundary-layer instability waves. Receptivities to freestream entropy waves with different frequencies and incident angles are studied. Receptivities to freestream entropy waves at frequency $F = 6.46 \times 10^{-5} (f^* = 100kHz)$ with different incident angles are studied first, followed by receptivities of entropy waves with incident angle $\theta_\infty = 39.7°$ at different frequencies.

Entropy Waves with $F = 6.46 \times 10^{-5}$

Boundary-layer receptivity to planar freestream entropy waves at frequency $F = 6.46 \times 10^{-5}$ with four different incident angles, i.e., $\theta_\infty = -5.3°, 17.2°, 39.7'$ and 62.2' are studied. The amplitude of the disturbance in freestreain is chosen to be $\epsilon = 1.0 \times 10^{-5}$, i.e., $\rho' = \epsilon M_\infty$. The receptivity mechanisms of boundary-layer normal modes *to* freestreain entropy waves and effect froin incident wave angles are analyzed.

Figure 41 shows the evolution of boundary-layer disturbances generated by freestream entropy waves at different incident wave angles. Except for $\theta_\infty = 62.2°$, there are smooth growths of the second-mode waves induced by freestream entropy waves with different incident angles. There are strong oscillations shown in the case with $\theta_\infty = 62.2°$, which results from modulation between second-mode waves and fast acoustic waves.

Figure 42 compares phase velocity of boundary-layer disturbances induced by entropy waves at $\theta_\infty = 39.7'$ with LST results. It shows that mode I waves are generated due to synchronization with fast acoustic waves near the leading edge. According to Ribner [10], Anyiwo and Bushnell [11], and Mckenzie and Westphal's study [12], the interaction between freestream disturbances and the oblique shock generates all three kinds of disturbance waves, i.e., acoustic waves, vorticity waves and entropy waves, irrespective of the nature of the freestream disturbance waves. Therefore, the generation of boundary-layer disturbances by freestream entropy waves are mainly through the fast acoustic waves generated behind the shock due to the interaction between shock waves and freestream entropy waves. In the receptivity process, the entropy waves generate fast acoustic waves froin interaction with the shock first. In turn, fast acoustic waves induce boundary-layer disturbances. During propagation downstream, mode I waves convert to Mack-mode waves after the synchronization point between mode I waves and the first-mode waves. Because there is no pressure perturbations in freestream, response coefficient defined in Eqn. 9 is not valid for receptivity to freestream entropy waves. To quantitatively study the second-mode receptivity of the boundary layer to freestream entropy waves, the response coefficient is redefined as

$$K_s = \frac{|p'_{II}|}{\epsilon p_\infty}, \tag{13}$$

where $|p'|_{II}$ is the maximum amplitude of pressure perturbations a.t the second-mode Branch II neutral point.

Figure 43 shows the effect of incident angle on response coefficient defined in Eqn. 13. For different inci-

Table 7: Response coefficients of the second mode to freestream entropy waves.

n	f_n^* (kHz)	K_s	$s_{II}^*(m)$	ω_{II}
7	104.5	265.9	0.5413	0.1454
8	119.4	133.3	0.4073	0.1442
9	134.3	93.68	0.3166	0.1430
10	149.2	63.92	0.2593	0.1438
11	164.1	31.60	0.2103	0.1424
12	179.1	34.26	0.1698	0.1397
13	194.0	36.17	0.1516	0.1429
14	208.9	27.33	0.1203	0.1371
15	223.8	19.18	0.1091	0.1399

dent angles of freestream entropy waves, the wave angles and amplitudes of the generated fast acoustic waves are different, which lead to different results of boundary-layer disturbances. It shows that there is significant drop in response coefficient with increasing incident angles.

Entronv waves at different frequencies

In this section, boundary-layer receptivity to freestream entropy waves with 15 different frequencies is studied. Freestream planar entropy waves at $\theta_\infty = 39.7'$ contain 15 frequencies with the lowest frequency of $f_1^* = 14.922kHz$ corresponding to dimensionless frequency of $F_1 = 9.63 \times 10^{-6}$. The perturbations of an arbitrary flow variable in the freestream are described in Eqn. 10 and satisfy relation of entropy waves. The relative amplitude and phase angle of entropy waves at different frequencies are given in in table 3. The overall wave amplitude is $\varepsilon = 1.0 \times 10^{-4}$, i.e., $\rho' = \epsilon M_\infty$.

Figure 44, 45 and 46 show the evolution of boundary-layer disturbances characterized by pressure perturbations along the wall surface induced by planar freestream entropy waves at $\theta_\infty = 39.7'$ with different frequencies. Similar to receptivity to fast acoustic waves shown in Fig. 28, 29 and 30, there are strong oscillations in boundary-layer disturbances at low frequencies within $1 \leq n \leq 5$(Fig. 44), where mode I waves are generated and modulated by fast acoustic waves, and at high frequencies within $11 \leq n \leq 15$(Fig. 46), where the second-mode waves are modulated by fast acoustic waves in downstream region after $s^* > 0.16m$. At middle frequencies within $6 \leq n \leq 10$ (Fig. 45), the boundary-layer disturbances are strongly amplified so that oscillations from modulation with fast acoustic waves are invisible. The response coefficients of the second mode at frequencies within $7 \leq n \leq 15$ are given in table 7.

Again, it shows in the table 7 that the second-mode Branch II neutral points are located at about $\omega_{II} = 0.14$, and the relative change in terms of ω ($w = R * F$) from the simulations is less than %5.

Figure 47 shows the effect on the second-mode response coefficient from change of frequencies. Overall, the second-mode response coefficients decrease as frequency increases, although the decrease is no not monotonic due to the effect of modulation.

Figure 48 and 49 compare distribution of phase velocity of boundary-layer disturbances induced by freestream entropy waves a.t two different frequencies ($n = 5, 7$) with the simulation result of mode I waves introduced from the inlet as well as the results from the LST. There is good agreement in distribution of phase velocity between simulation results from different type of forcing disturbances. It shows that the second-mode receptivity to freestream entropy waves are very similar to receptivity to freestream fast acoustic waves shown in Fig. 35. Therefore, the fast acoustic waves generated behind the shock due to the interaction between shock waves and freestream entropy waves plays a critical role in the receptivity to freestream entropy waves.

Receptivity to Planar Freestream Vorticity Waves

In freestream, vorticity waves associate with velocity fluctuation. In this section, boundary-layer receptivity to planar freestream vorticity waves are revisited for Mach 8.0 flow over the 5.3' half-angle sharp wedge. Effect from incident angle and frequency on receptivity to freestream vorticity waves are studied.

Vorticity Waves with $F = 6.46 \times 10^{-5}$

Boundary-layer receptivity to planar freestream vorticity waves a.t frequency $F = 6.46 \times 10^{-5}$ with four different incident angles, i.e., $\theta_\infty = -5.3°, 17.2°, 39.7'$ and $62.2°$ are studied. The amplitude of the disturbance in freestream is chosen to be $\varepsilon = 1.0 \times 10^{-5}$. The evolution of boundary-layer disturbances induced by freestreain vorticity waves with different incident wave angles is plotted in Fig. 50. It shows that there are smooth growths of the second-mode waves induced by freestream vorticity waves with different incident angles. The second-mode response coefficients defined in Eqn. 13 for different incident angles are plotted in Fig. 51. Similar to results of entropy waves shown in Fig. 43, the second-mode response coefficient decrease dramatically with increasing incident angles.

Figure 52 compares the initial evolutions of boundary-layer disturbances induced by different type of freestream disturbances. It shows that there are very similar growth and decay patterns in evolutions of boundary-layer disturbances induced by freestream fast acoustic, entropy and vorticity waves, while the development of boundary-layer disturbances by freestream slow acoustic waves is totally different from the other three freestream waves. It indicates that there are similar the receptivity mechanisms involved in receptiv-

ity process to freestream fast acoustic waves, entropy waves and vorticity waves. This is because the interaction between freestream disturbances and the oblique shock generates all three kinds of disturbance waves, i.e., acoustic waves, vorticity waves and entropy waves, irrespective of the nature of the freestream disturbance waves, although the magnitudes of different components of different type of waves generated behind the shock are different depending on the type and incident angle of disturbances in freestream and angle of oblique shock as well as freestream mean flow conditions. In current studies of receptivity to freestream entropy waves and vorticity waves with four different incident angles, the results shows that the generated acoustic waves behind the shock belong to fast acoustic waves. Based on Mckenzie and Westphal's theory [12], the wave angle of generated fast acoustic waves behind the shock by freestream vorticity waves is same as that by freestream entropy waves only if the incident angles in freestream are same, although the amplitude of generated fast acoustic waves might be different. The generation of the second-mode waves are mainly through resonant interaction between mode I waves and fast acoustic waves if there are no slow acoustic waves in the flow field. Therefore, there should be very similar receptivity process between receptivity to freestream entropy waves and vorticity waves. However, there is much difference in distribution of phase velocity of boundary-layer disturbances in the upstream region induced by freestream vorticity waves with $\theta_\infty = 39.7'$ compared with that by freestream entropy waves shown in Fig. 53, although they merge together and approach to phase velocity curve of the second-mode waves in downstream region. The difference may be because there are strong interactions between boundary-layer disturbances and forcing vorticity waves in receptivity to freestream vorticity waves.

Figure 54 compares the growth rates of boundary-layer disturbances induced by freestream disturbaiices with LST results. It shows that there is acceptable agreement in the second-mode unstable region between simulation results and LST results. Compared with the second-mode growth rates shown in Fig. 37 and 38, it is possible to obtain rational second-mode growth rates in studying boundary-layer disturbances induced by freestream slow acoustic waves, entropy waves or vorticity waves in experiment, although it is difficult to compare growth rates from receptivity to fast acoustic waves with LST results.

Vorticity waves at different frequencies

In this section, boundary-layer receptivity to freestream vorticity waves with 15 different frequencies is studied. Freestream planar vorticity waves at $\theta_\infty = 39.7'$ contain 15 frequencies with the lowest frequency of $f_1^* = 14.922kHz$ corresponding to dimensionless frequency of $F_1 = 9.63 \times 10^{-6}$. The perturbations of an arbitrary flow variable in the freestream are described in Eqn. 10 and satisfy relation of vorticity waves. The relative amplitude and phase angle of vorticity waves at different frequencies are given in in table 3. The overall wave amplitude is $\varepsilon = 1.0 \times 10^{-4}$.

Table 8: Response coefficients of the second mode to freestream vorticity waves

n	f_n^* (kHz)	K_s	$s_{II}^*(m)$	ω_{II}
7	104.5	624.0	0.5443	0.1459
8	119.4	318.0	0.4046	0.1437
9	134.3	194.3	0.3146	0.1426
10	149.2	131.1	0.2528	0.1420
11	164.1	76.04	0.2131	0.1434
12	179.1	58.86	0.1736	0.1412
13	194.0	52.31	0.1503	0.1423
14	208.9	43.31	0.1251	0.1398
15	223.8	32.23	0.1123	0.1420

Figure 55, 56 and 57 compared amplitudes of pressure perturbations along the wall surface induced by planar freestream vorticity waves at $\theta_\infty = 39.7'$ with different frequencies, which are very similar to the evolution of disturbances generated by freestream entropy waves shown in Fig. 44, 45 and 46. There are strong oscillations in boundary-layer disturbances at low frequencies within $1 \leq n \leq 5$(Fig. 44), where mode I waves are generated and modulated by fast acoustic waves, and at high frequencies within $11 \leq n \leq 15$(Fig. 46), where the second-mode waves are modulated by fast acoustic waves in downstream region after $s^* > 0.16m$. In addition, the second-mode waves at frequencies within $6 \leq n \leq 8$ are so strongly amplified so that there is effect from high-order harmonics on amplitudes of pressure perturbations at high frequencies within $12 \leq n \leq 15$ in the downstream region after $s^* > 0.4m$. Obviously, the oscillations resulting from wave modulations has much longer wave length than that from effect of high-order harmonics. The response coefficients of the second mode at frequencies within $5 \leq n \leq 15$ are given in table 8.

As expected, that the second-mode Branch II neutral points are located at about $\omega_{II} = 0.14$, and the relative change in terms of w $(\omega = \mathrm{R} * \mathbf{F})$ from the simulations is less than %5. The second-mode response coefficients drop off significantly as frequency increases, which is also shown in Fig. 58.

Conclusions

The receptivity mechanisms of hypersonic boundary-layer to freestream fast acoustic waves, slow acoustic waves, entropy waves and vorticity waves are studied by numerical simulations. Boundary-layer normal modes

induced by freestream disturbances are identified by comparing with LST results. The effects of incident wave angles and frequencies, on the receptivity are studied.

In the receptivity process to fast acoustic waves, inode I waves are generated and amplified near the leading edge due to resonant interaction between mode I waves and forcing fast acoustic waves. During propagation downstream, mode I waves convert to the second mode waves at the synchronization point between mode I and the second mode. The forcing fast acoustic waves do not interact directly with the unstable Mack modes. Instead, the stable mode I plays an important role in the receptivity process because they interact with both the forcing acoustic waves and the unstable Mack modes. Through the interactions, the stable mode I transfers the wave energy from the forcing freestream fast acoustic waves to the second Mack-mode waves.

Unlike forcing fast acoustic waves, the forcing slow acoustic waves can directly generate Mack-mode waves without exchanging energy with stable boundary-layer normal modes because there is resonant interaction between the first-mode waves and slow acoustic waves. For freestream acoustic waves with incident angle smaller than 45°, the second-mode receptivity to freestream slow acoustic waves are several times stronger than that to fast acoustic waves.

For receptivity to freestream entropy waves or vorticity waves, the generation of boundary-layer disturbances are mainly through fast acoustic waves generated behind the shock due to the interaction between shock waves and freestream disturbances.

Ackiiowledgemeiits

This research was supported by the Air Force Office of Scientific Research, USAF, under AFOSR Grand # F49620-00-1-0101. The program manager is Dr. John Schmisseur. The views and conclusions contained herein are those of the author and should not be interpreted as necessarily representing the official policies or endorsements either expressed or implied, of the Air Force Office of Scientific Research or the U.S. Government.

References

[1] Th. Herbert and M. V. Morkovin. Dialogue on Bridging Some Gaps in Stability and Transition Research. *In Laminar-Turbulent Transition, IUTAM Symposium, Stuttgart, Germany, 1979, R. Eppler, H. Fasel, Editors, pp. 47–72,* Springer-Verlag Berlin, 1980.

[2] M. V. Morkovin and E. Reshotko. Dialogue on Progress and Issues in Stability and Transition Research. *In Laminar-Turbulent Transition. IUTAM Symposium, Toulouse, France, 1989, D. Arnal, R. Michel, Editors,* Springer-Verlag Berlin, 1990.

[3] E. Resliotko. Boundary Layer Instability, Transition and Control. *AIAA paper 94-0001,* 1994.

[4] Th. Herbert. Progress in Applied Transition Analysis. *AIAA paper 96-1993,* 27th AIAA Fluid Dynamics Conference, New Orleans, LA, June, 1996.

[5] M. Morkovin. On the Many Faces of Transition. *Viscous Drag Reduction,* C.S. Wells, editor, Plenum, 1969.

[6] M. E. Goldstein and L. S. Hultgren. Boundary-Layer Receptivity to Long-Wave Free-Stream Disturbances. *Annual Review of Fluid Mechanics,* Vol. 21, pp. 137-166 1989.

[7] R. Lin M. R. Malik and R. Sengupta. Computation of Hypersonic Boundary-Layer Response to External Disturbances. *AIAA paper 99-0411,* 1999.

[8] *Y.* Ma and X. Zhong. Receptivity to freestream disturbances of mach 4.5 flow over a flat plate. AIAA Paper 2002-0140, AIAA, 2002.

[9] L. M. Mack. Stability of Axisymmetric Boundary Layers on Sharp Cones at Hypersonic Mach Numbers. *AIAA Paper 87-1413,* 1987.

[10] H. S. Ribner. Shock-turbulence interaction and the generation of noise. *NACA* TR *1233,* 1954.

[11] J. C. Anyiwo and D. M. Bushnell. Turbulence amplification in shock-wave boundary-layer interaction. *AIAA Journal,* 20(7):893–899, July 1982.

[12] J. F. Mckenzie and K. O. Westphal. Interaction of linear waves with oblique shock waves. *The Physics of Fluids,* 11(11):2350–2362, November 1968.

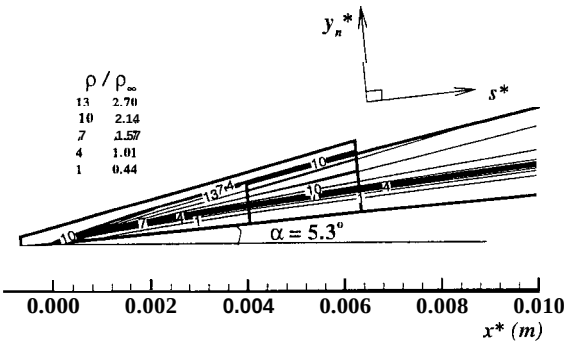

Figure 1: Contours of density near the leading edge for steady base flow.

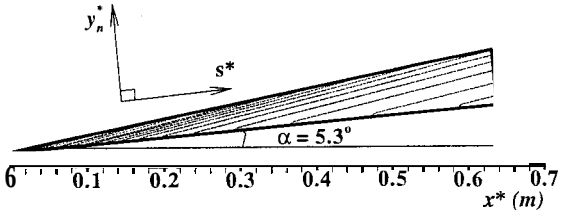

Figure 2: Contours of pressure for steady base flow.

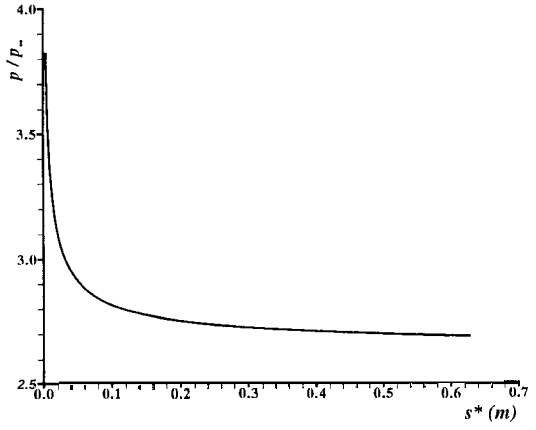

Figure **3:** Distribution of pressure along the wall surface for steady base flow over the wedge.

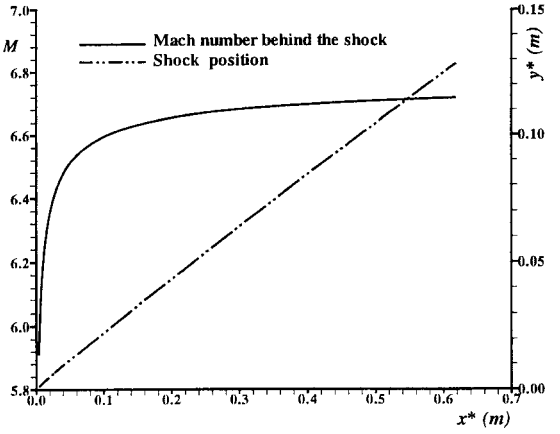

Figure **4:** Shock position and distribution of Mach number behind the shock for steady base flow over the wedge.

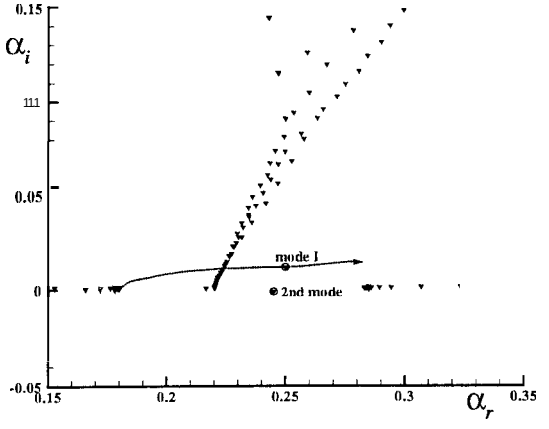

Figure 5: Spectra of eigenvalues with $\mathrm{F} = 9.63 \times 10^{-5}$ at station $\mathrm{R} = 2287.0$ $(w = R * F = 0.2203)$.

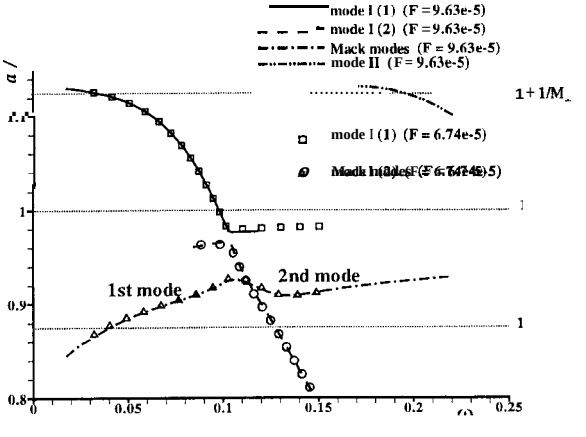

Figure 6: Distribution of phase velocities of boundary-layer normal inodes as a function of w at different frequencies.

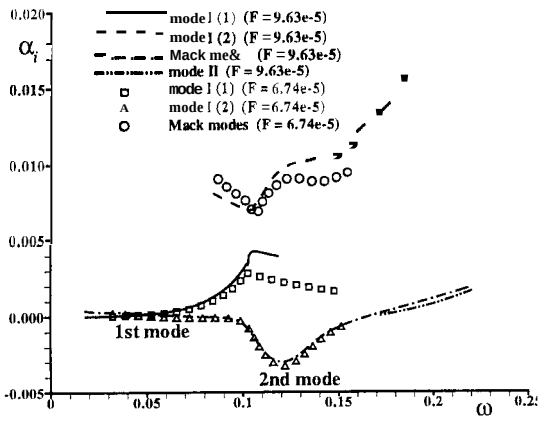

Figure 7: Distribution of growth rates of boundary-layer normal modes as a function of ω at different frequencies.

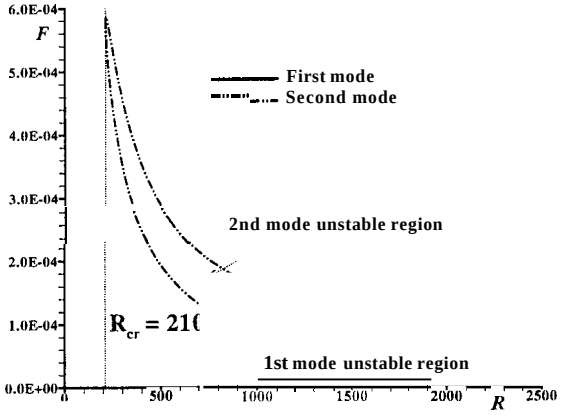

Figure 8: Neutral stability curves of two-dimensional first and second inodes in the hypersonic flow over the wedge.

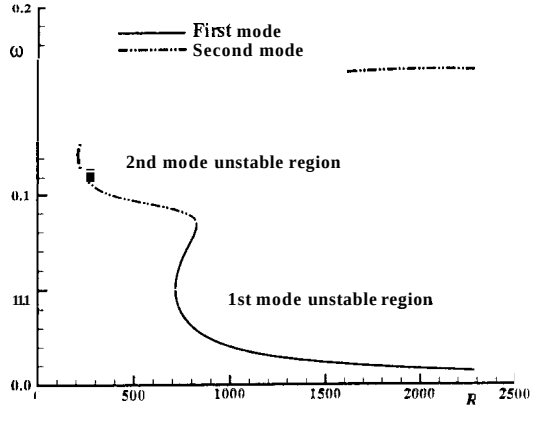

Figure 9: Neutral stability curves of two-dimensional first and second modes in the hypersonic flow over the sharp wedge.

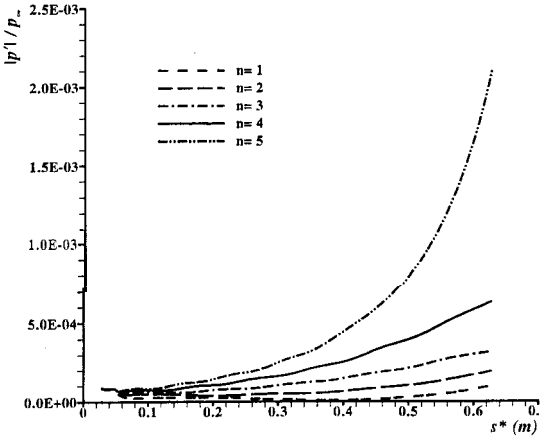

Figure 10: Comparison of presure perturbations of Mack modes along the wall surface at different frequencies.

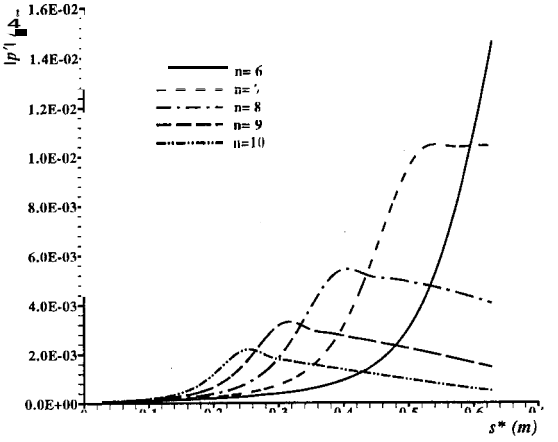

Figure 11: Comparison of presure perturbations of Mack modes along the wall surface at different frequencies.

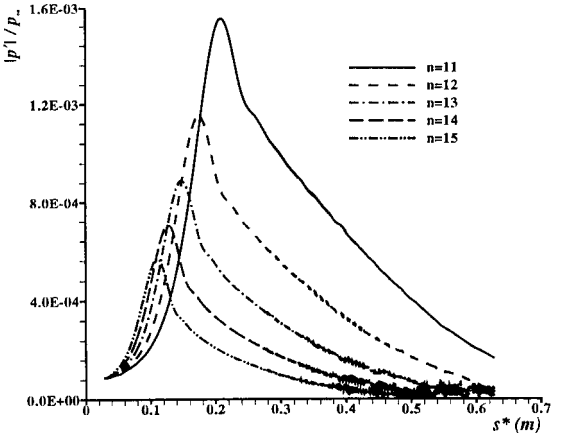

Figure 12: Comparison of presure perturbations of Mack modes along the wall surface at different frequencies.

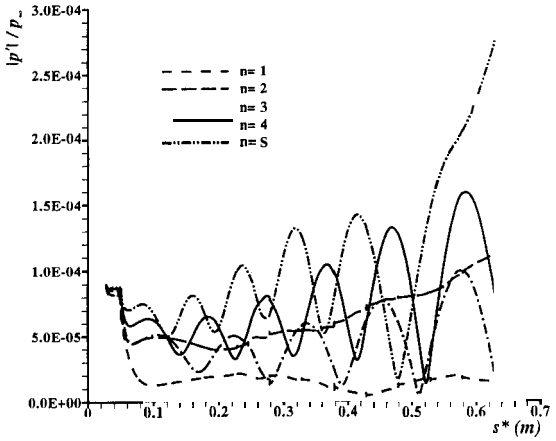

Figure 13: Comparison of presure perturbations along the wall surface for the cases of imposed mode I of different frequencies at the inlet.

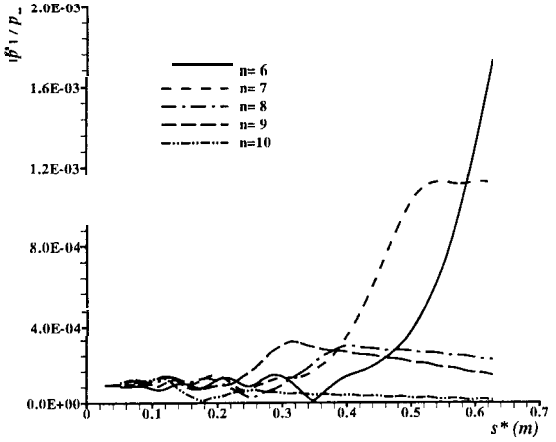

Figure 14: Comparison of presure perturbations along the wall surface for the cases of imposed mode I of different frequencies at the inlet.

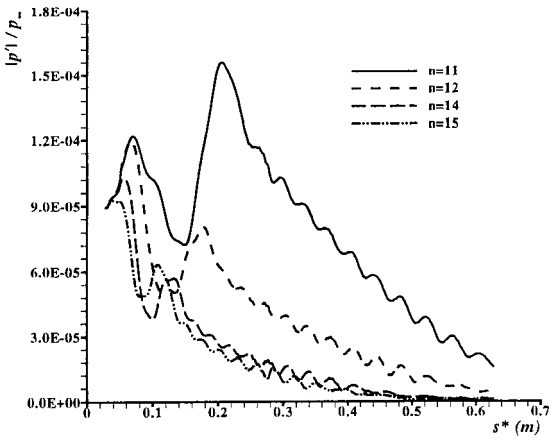

Figure 15: Comparison of presure perturbations along the wall surface for the cases of imposed mode I of different frequencies at the inlet.

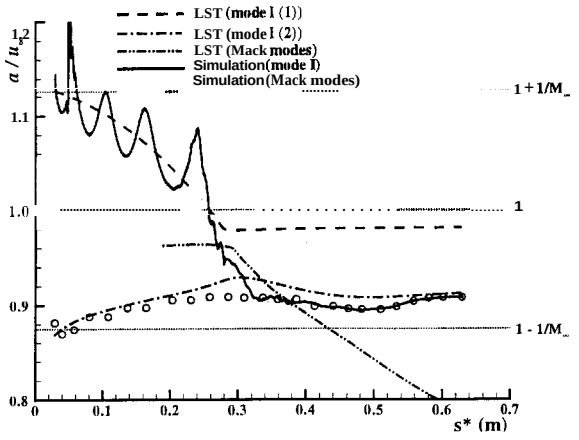

Figure 16: Comparison of phase velocities of boundary normal modes from numerical simulations with LST results ($F = 6.74 \times 10^{-5}$, n = 7).

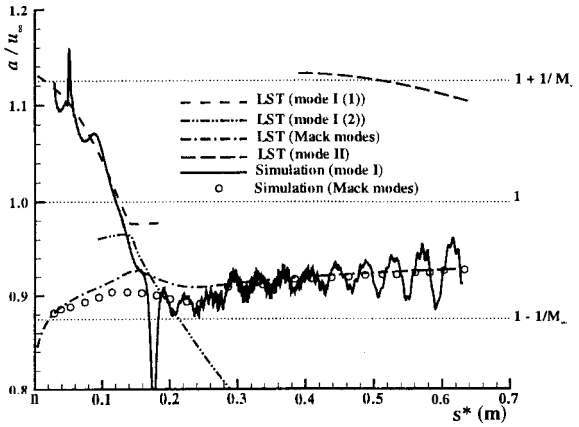

Figure 17: Coinparison of phase velocities of boundary-layer normal modes from numerical simulations with LST results ($F = 9.63 \times 10^{-5}$, n = 10).

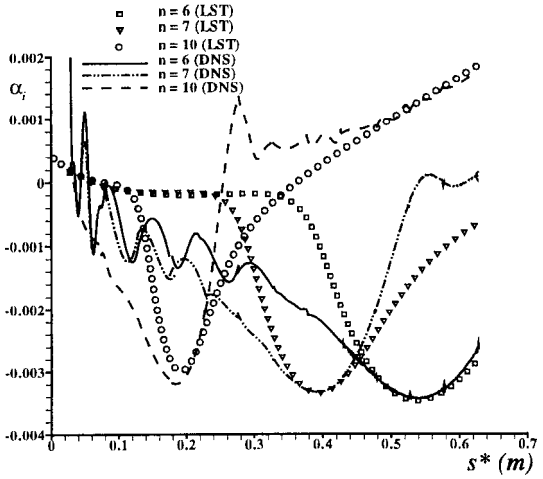

Figure 18: Comparison of growth rates of Mack modes between numerical simulation results and LST results.

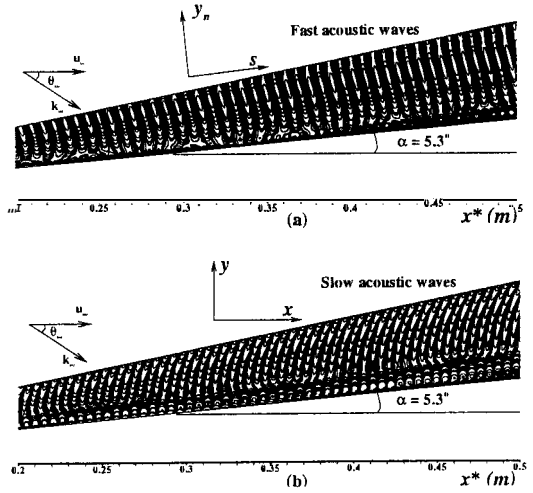

Figure 19: Contours of pressure perturbations due to freestream plane acoustic waves ($\theta_\infty = -5.3°$ and $F = 6.46 \times 10^{-5}$).

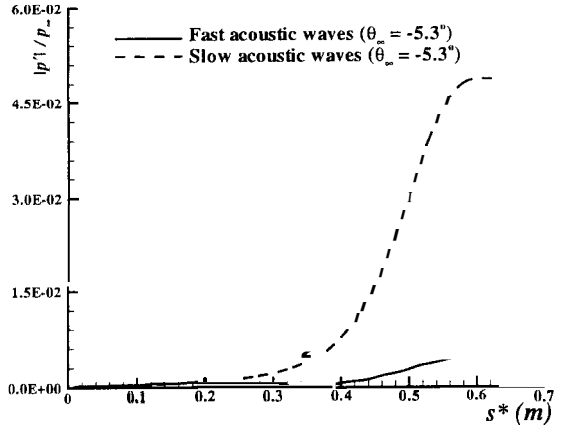

Figure 20: Distribution of pressure perturbations on the wall due to freestream plane acoustic waves ($\theta_\infty = -5.3°$ and $F = 6.46 \times 10^{-5}$).

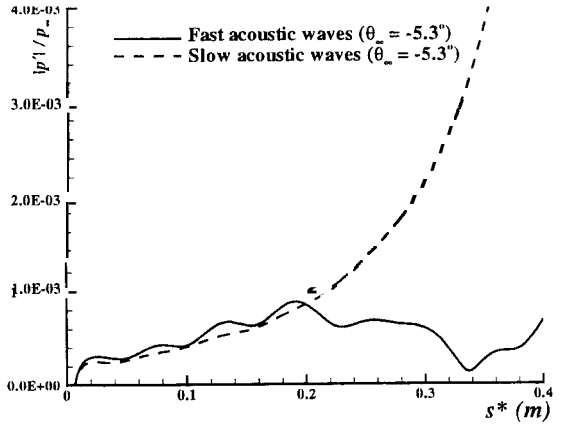

Figure 21: Distribution of pressure perturbations on the wall due to freestream plane acoustic waves ($\theta_\infty = -5.3°$ and $F = 6.46 \times 10^{-5}$).

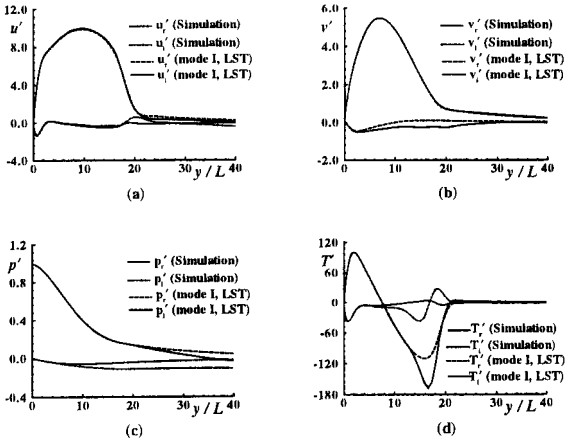

Figure 22: Comparison of disturbance structures induced by freestream fast acoustic waves with mode I from the LST at $x^* = 0.1178m$, $R = 1207.6$.

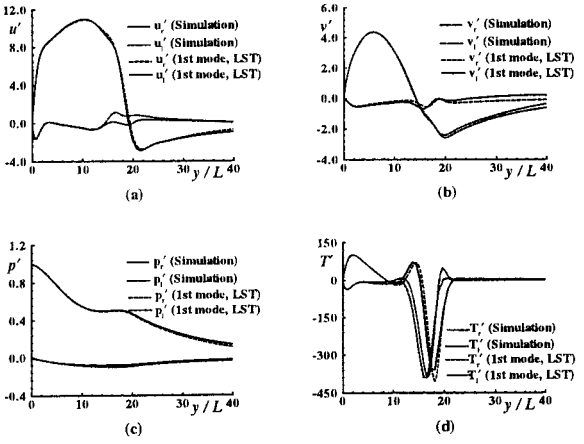

Figure 23: Comparison of disturbance structures induced by slow acoustic waves with the second mode from the LST at $x^* = 0.1178m$, $R = 1207.6$.

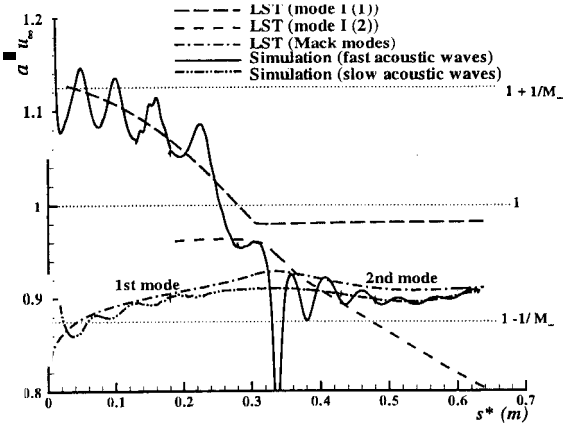

Figure 24: Distribution of phase velocities of boundary-layer disturbances due to freestream plane slow acoustic waves and comparison with that due to fast acoustic waves ($\theta_\infty = -5.3°$ and $F = 6.46 \times 10^{-5}$).

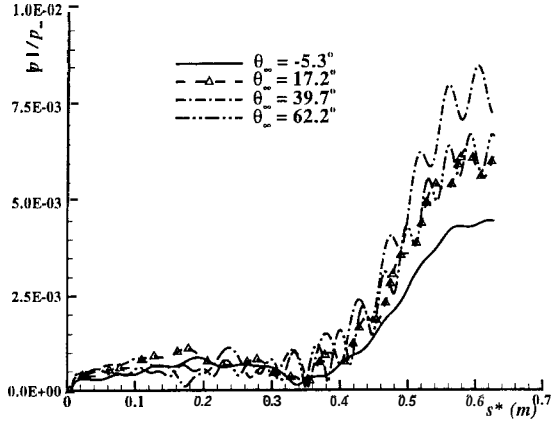

Figure 25: Distributions of pressure perturbations on the wall due to freestream plane fast acoustic waves at different incident angles ($F = 6.46 \times 10^{-5}$).

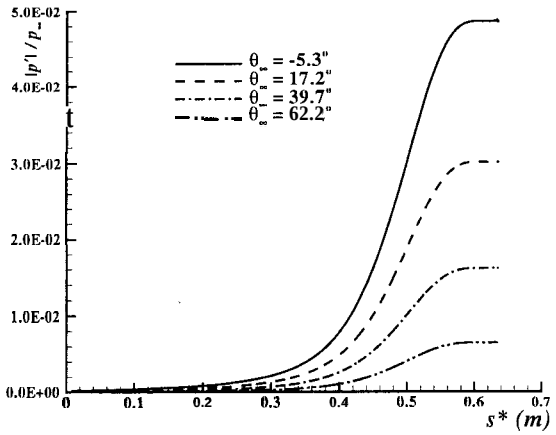

Figure 26: Distributions of pressure perturbations on the wall due to freestream plane slow acoustic waves at different incident angles ($F = 6.46 \times 10^{-5}$).

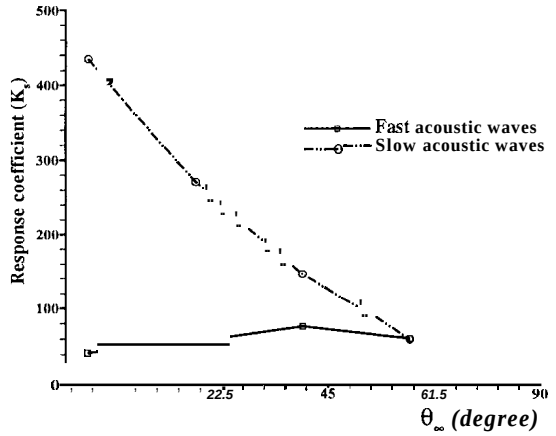

Figure 27: Response coefficients of the second mode to freestream acoustic waves vs. incident wave angles ($F = 6.46 \times 10^{-5}$).

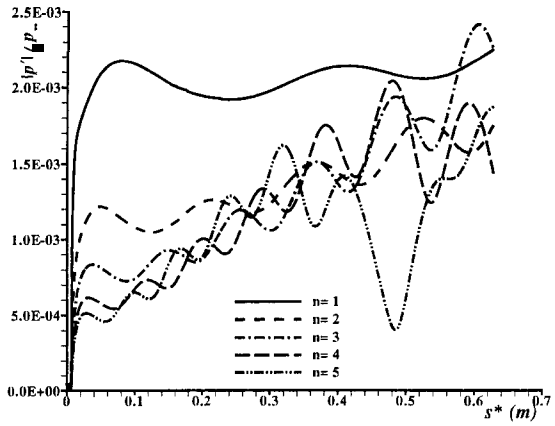

Figure 28: Comparison of presure perturbations along the wall surface due to freestream plane fast acoustic waves at different frequencies.

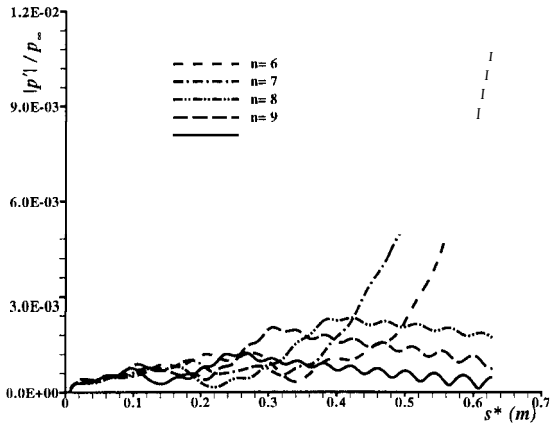

Figure 29: Comparison of presure perturbations along the wall surface due to freestream plane fast acoustic waves at different frequencies.

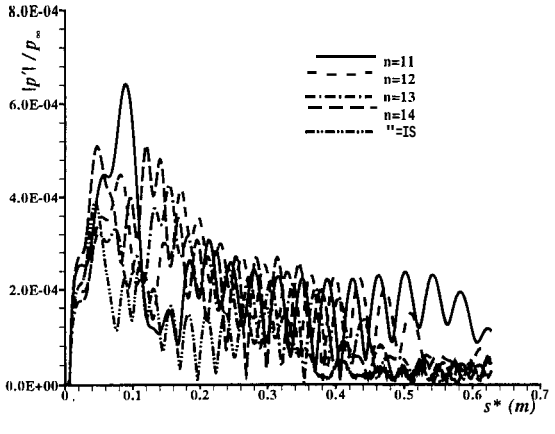

Figure 30: Comparison of presure perturbations along the wall surface due to freestream plane fast acoustic waves at different frequencies.

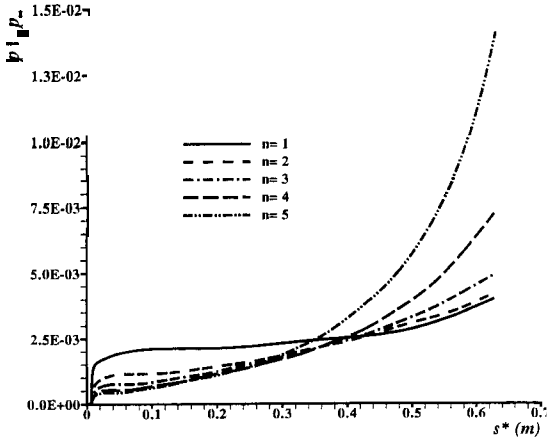

Figure 31: Comparison of presure perturbations along the wall surface due to freestream plane slow acoustic waves at different frequencies.

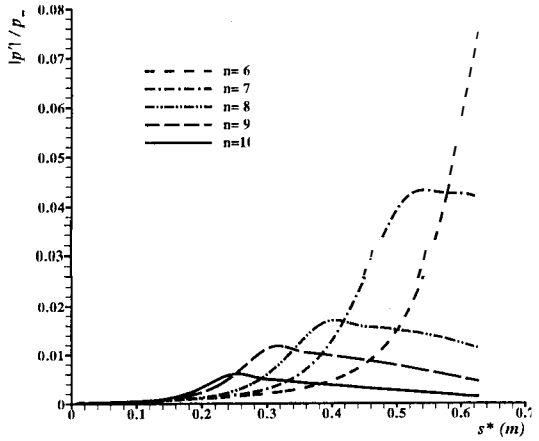

Figure 32: Comparison of presure perturbations along the wall surface due to freestream plane slow acoustic waves at different frequencies.

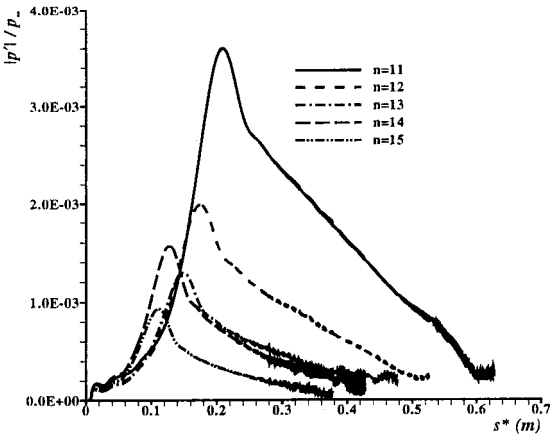

Figure 33: Comparison of presure perturbations along the wall surface due to freestream plane slow acoustic waves at different frequencies.

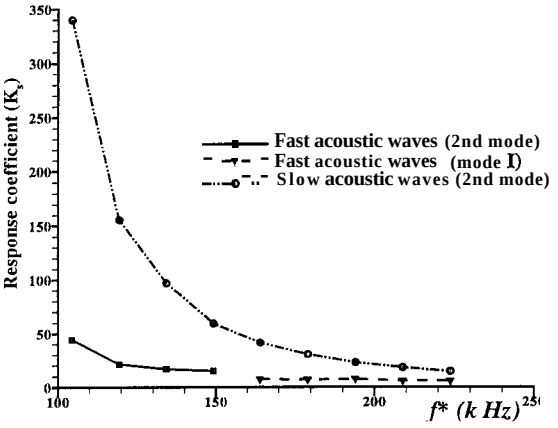

Figure 34: Comparison of the second-mode response coefficients to freestream acoustic waves at different frequencies.

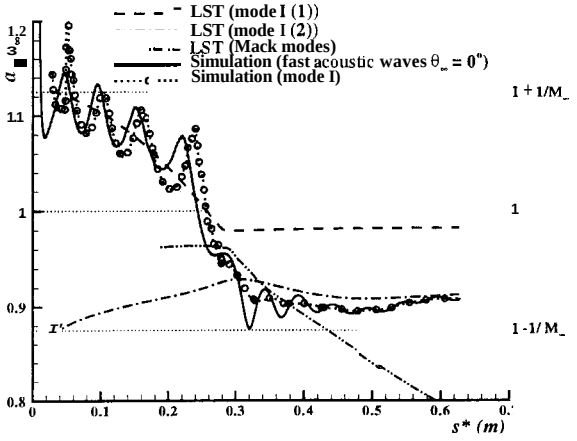

Figure 35: Comparison of phase velocities of boundary-layer disturbances from numerical simulations with LST results ($F = 6.74 \times 10^{-5}$, n = 7).

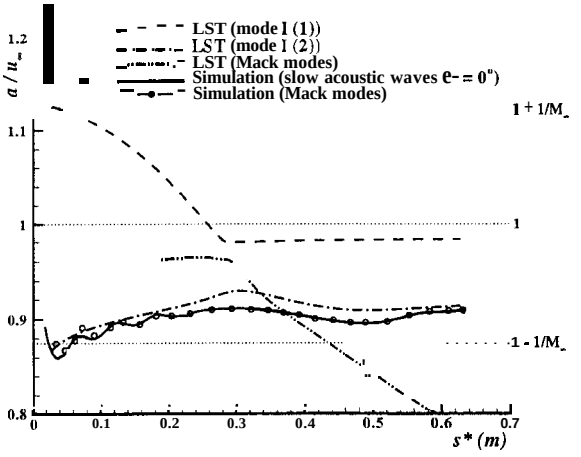

Figure 36: Comparison of phase velocities of boundary-layer disturbances from numerical simulations with LST results ($F = 6.74 \times 10^{-5}$, n = 7).

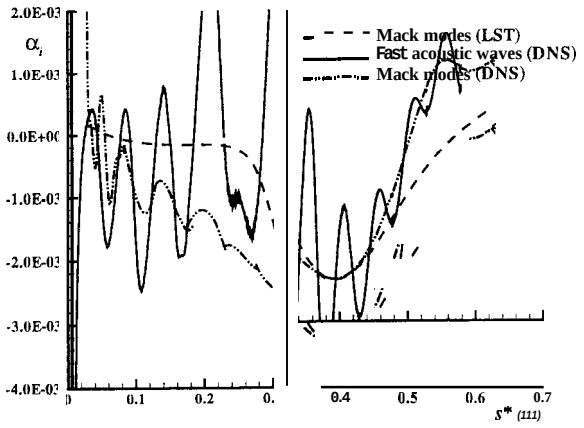

Figure *37:* Comparison of growth rates of boundary-layer disturbances from numerical simulations with LST results ($F = 6.74 \times 10^{-5}$, $n = 7$).

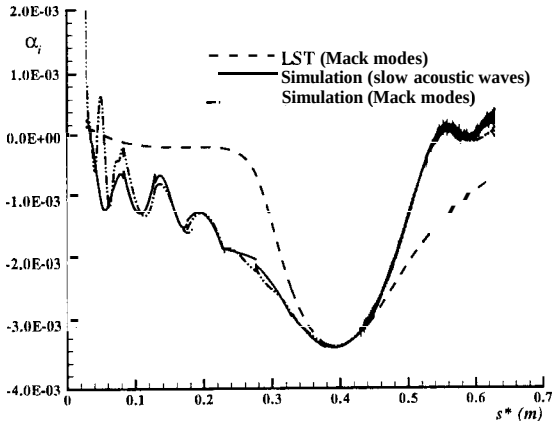

Figure **38:** Comparison of phase velocities of boundary-layer disturbances from numerical simulations with LST results ($F = 6.74 \times 10^{-5}$, $n = 7$).

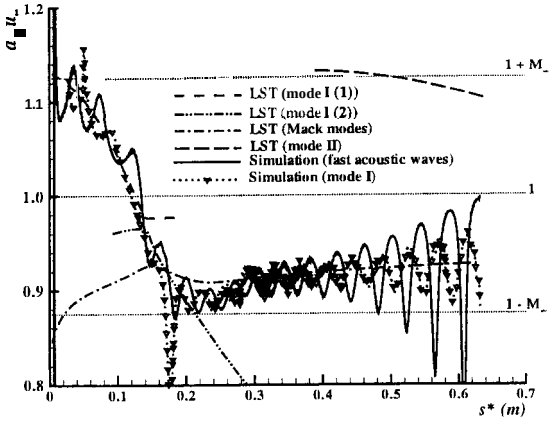

Figure 39: Comparison of phase velocities of boundary-layer disturbances from numerical simulations with LST results ($F = 9.63 \times 10^{-5}$, $n = 10$).

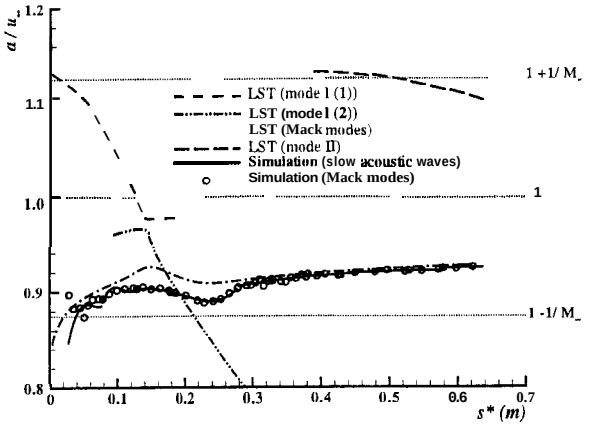

Figure 40: Comparison of phase velocities of boundary-layer disturbances from numerical siinulations with LST results ($F = 9.63 \times 10^{-5}$, $n = 10$).

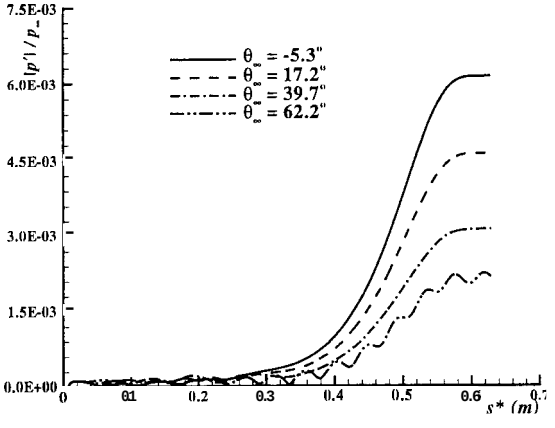

Figure 41: Distributions of pressure perturbations on the wall due to freestream plane entropy waves at different incident angles ($F = 6.46 \times 10^{-5}$).

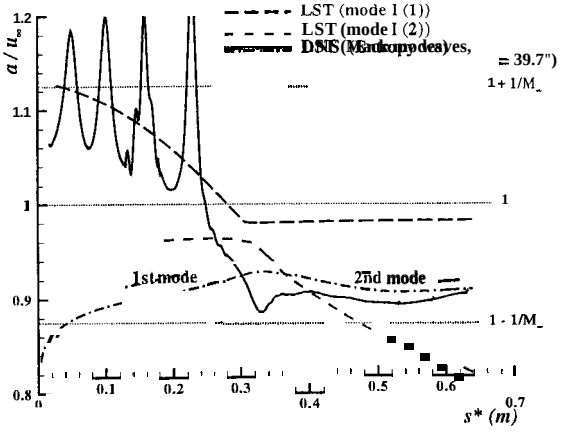

Figure 42: Distribution of phase velocities of boundary-layer disturbances due to plane entropy waves (θ_∞ = 39.7' and $F = 6.46 \times 10^{-5}$).

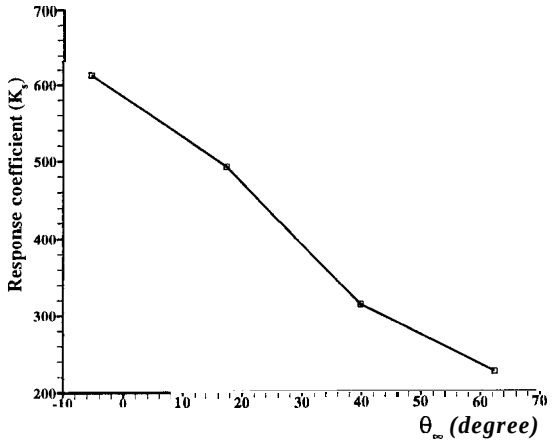

Figure 43: Response coefficients of the second mode to freestream entropy waves vs. incident wave angles ($F = 6.46 \times 10^{-5}$).

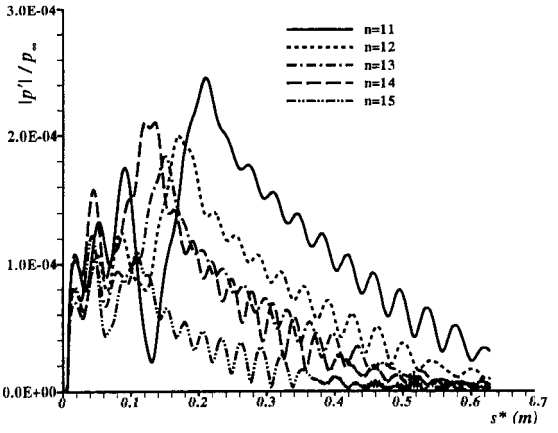

Figure 46: Comparison of presure perturbations along the wall surface due to freestream plane entropy waves at different frequencies.

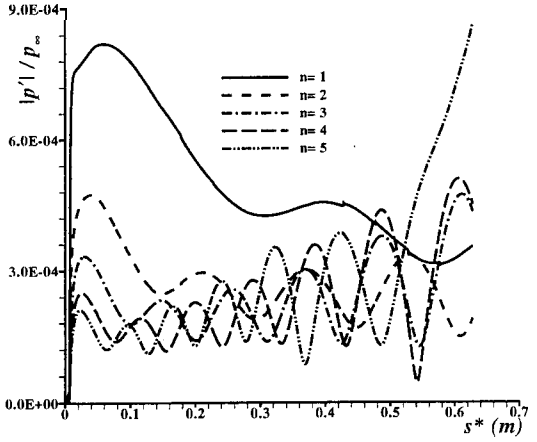

Figure 44: Comparison of presure perturbations along the wall surface due to freestream plane entropy waves at different frequencies ($\theta_\infty = 39.7'$).

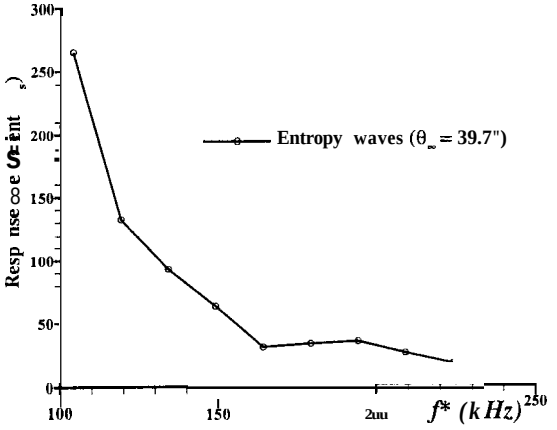

Figure 47: Comparison of the second-mode response coefficients to freestream entropy waves at different frequencies ($\theta_\infty = 39.7°$).

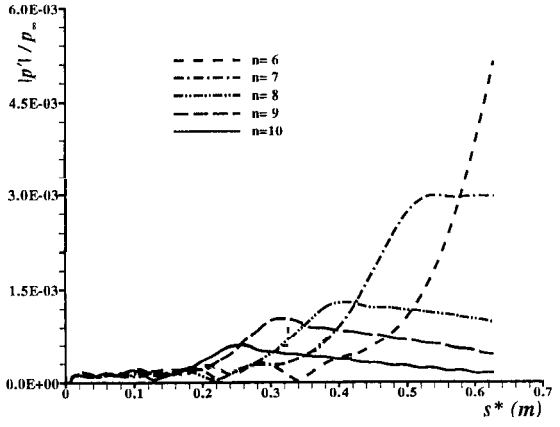

Figure 45: Comparison of presure perturbations along the wall surface due to freestream plane entropy waves at different frequencies ($\theta_\infty = 39.7'$).

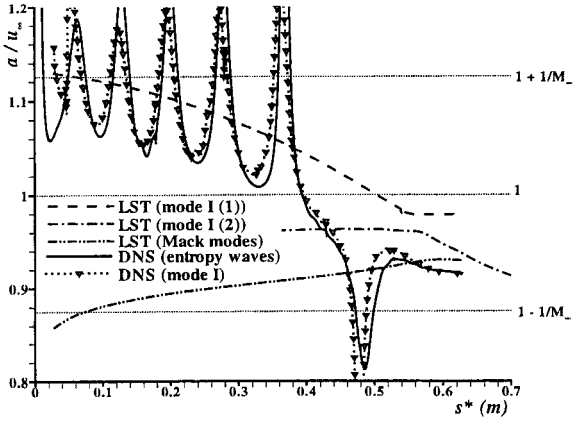

Figure 48: Comparison of phase velocities of boundary-layer disturbances from numerical simulations with LST results ($F = 4.81 \times 10^{-5}$, $n = 5$).

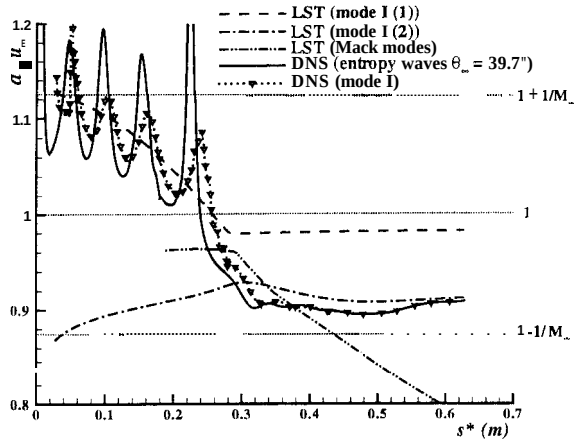

Figure 49: Comparison of phase velocities of boundary-layer disturbances from numerical simulations with LST results ($F = 6.74 \times 10^{-5}$, n = 7).

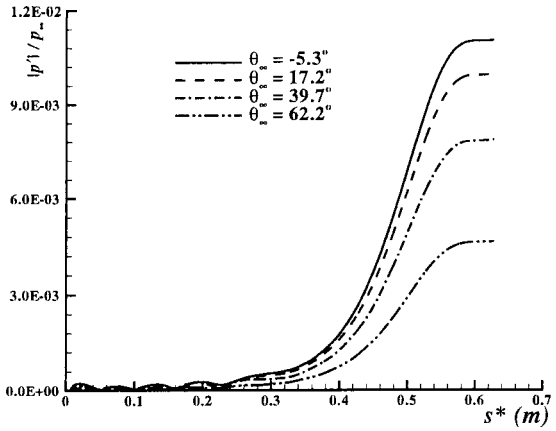

Figure 50: Distributions of pressure perturbations on the wall due to freestream plane vorticity waves at different incident angles ($F = 6.46 \times 10^{-5}$).

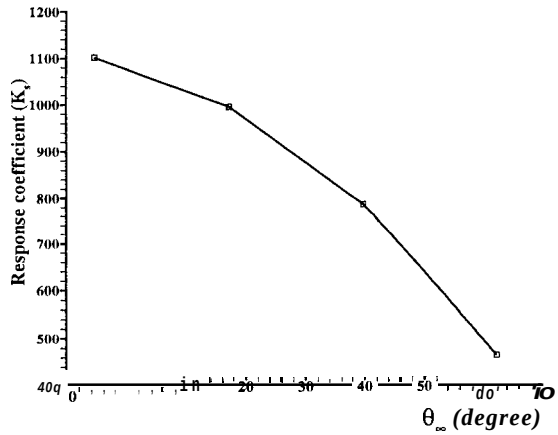

Figure 51: Response coefficients of the second mode to freestream vorticity waves vs. incident wave angles ($F = 6.46 \times 10^{-5}$).

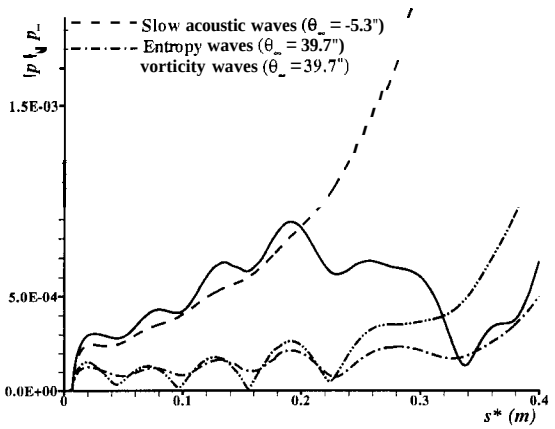

Figure 52: Distributions of pressure perturbations on the wall due to different freestream disturbances ($F = 6.46 \times 10^{-5}$).

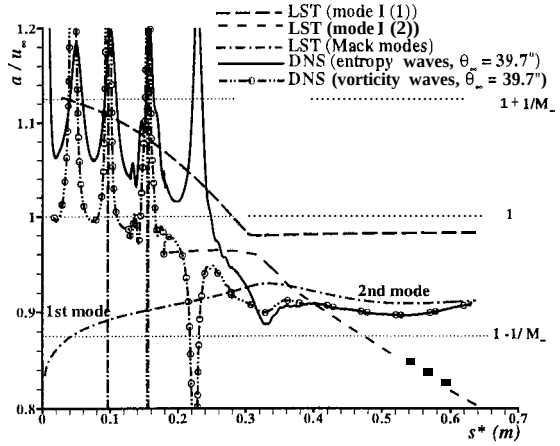

Figure 53: Comparison of phase velocities of boundary-layer disturbances due to planar vorticity waves with that due to planar entropy waves ($\theta_\infty = 39.7'$ and $F = 6.46 \times 10^{-5}$).

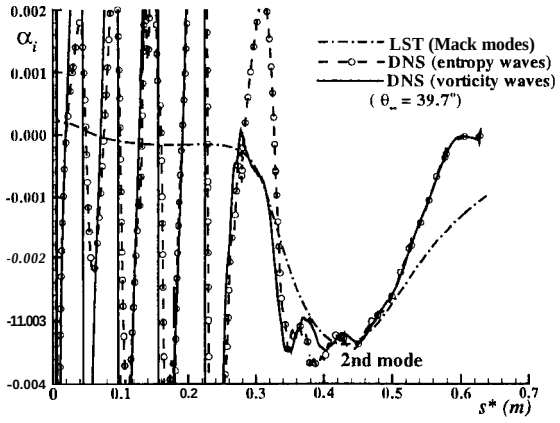

Figure 54: Comparison of growth rates of boundary-layer disturbances due to planar vorticity waves with that due to planar entropy waves ($\theta_\infty = 39.7'$ and $F = 6.46 \times 10^{-5}$).

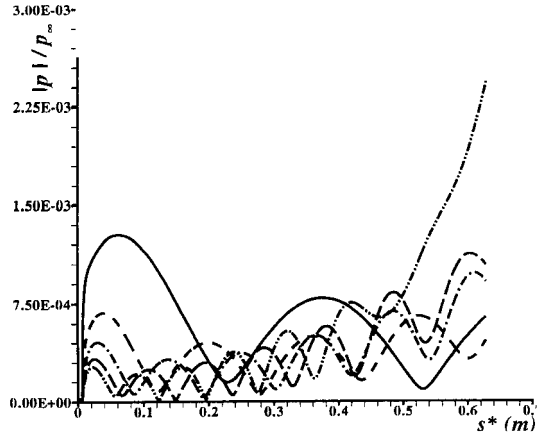

Figure 55: Comparison of presure perturbations along the wall surface due to freestream plane vorticity waves at different frequencies ($\theta_\infty = 39.7'$).

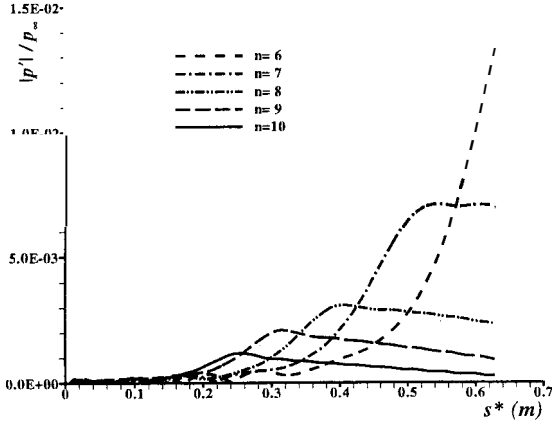

Figure 56: Comparison of presure perturbations along the wall surface due to freestream plane vorticity waves at different frequencies ($\theta_\infty = 39.7'$).

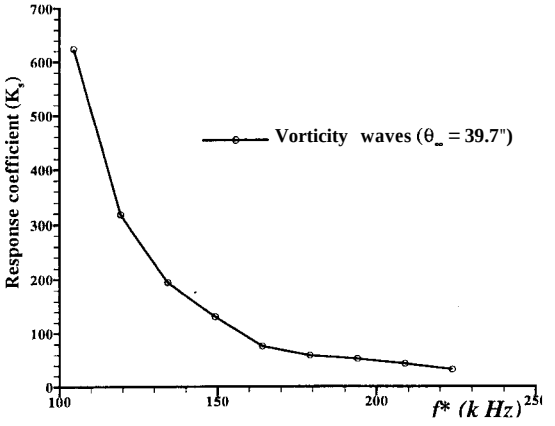

Figure 58: Comparison of the second-mode response coefficients to freestream vorticity waves at different frequencies ($\theta_\infty = 39.7'$).

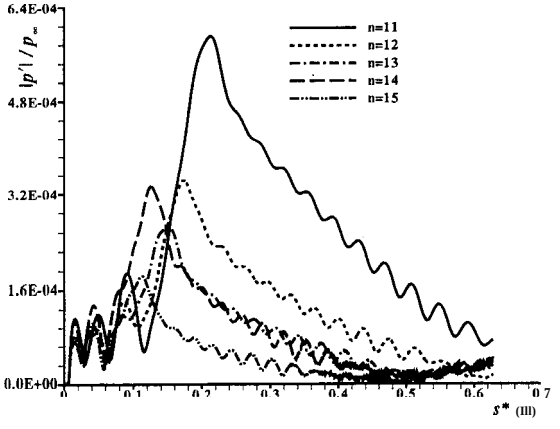

Figure 57: Comparison of presure perturbatioiis along the wall surface due to freestream plane vorticity waves at different frequencies ($\theta_\infty = 39.7'$).